UNIVERSITAT POLITÈCNICA DE VALÈNCIA

ESCUELA TÉCNICA SUPERIOR DE INGENIERÍA DEL DISEÑO

INSTITUTO UNIVERSITARIO CMT-MOTORES TÉRMICOS

COMPARATIVE STUDY OF AN INDIRECTLY COOLED BATTERY MODULE

Final Bachelor's Degree Project

Bachelor's Degree in Aerospace Engineering

Author: Joan Javier Ferrer García

Tutor: Xandra Marcelle Margot, Ph.D

Valencia, September, 2021

Acknowledgements

I would like to give a special thanks to my project supervisor, Xandra Marcelle Margot, for teaching me the necessary concepts for the completion of this thesis, and guiding me along the entire process.

Moreover, thanks to the *Universitat Politècnica de València*, for making my graduate studies a reality, and allowing me carry out this project.

I want to thank my family as well, for accompanying me throughout everything. Also, to my girlfriend Esther, who has always supported me and helped me become who I am today.

Valencia, September 2021

Joan Javier Ferrer García

Abstract

During the development of this project, a comparative study of the behavior of a cold-plate based indirectly cooled battery module is performed. The cell of the study is a Toshiba SCiB^{TM}. After an introduction to batteries and their working principle, a short discussion on the different models available in the ANSYS Fluent program is made, and the Equivalent Circuit Model (ECM) is used for the calculations. The design of the battery module and the indirect refrigeration system is based on a previous study and it is fully described. In that previous study, the effect of the cold-plate based refrigeration system on the module temperature was studied during a 4C discharge of the battery and an overall 2.5 kg/s mass flow. It showed that the module attained too high temperatures, whereby it could be concluded that the residence time of the fluid was very small and did not extract efficiently the generated heat. Therefore, in this project, the mass flow is reduced to achieve a better efficiency compared to the previous case. Additionally, in the previous study the electrical model parameters for the cell considered were not available, so the ones that come by default in ANSYS Fluent were used. In this study the real electrical parameters of the Toshiba SCiB^{TM} are used, and a complete study is done, in order to discuss the differences between both battery models. Finally, as an attempt to find another more efficient cooling strategy, an immersion based refrigeration system is proposed and simulated, and the differences between both refrigeration methods are studied.

Keywords: indirect cooling, cold-plate, battery module, Toshiba SCiB^{TM}, discharge, Equivalent Circuit Model, immersion cooling.

Resumen

Durante el desarrollo de este proyecto, se realiza un estudio comparativo del comportamiento de un módulo de baterías con refrigeración indirecta por placa fría. La celda estudiada es una Toshiba SCiB^{TM}. Después de una introducción sobre las baterías y su principio de funcionamiento, se incluye una breve discusión sobre los diferentes modelos disponibles en el programa ANSYS Fluent, y se utiliza el modelo de circuito equivalente (ECM) para los cálculos. El diseño del módulo de baterías y del sistema de refrigeración indirecta está basado un estudio previo que se describe aquí. En él se estudia el efecto del sistema de refrigeración para una descarga de la batería de 4C y un flujo másico total de 2.5 kg/s. Los resultados muestran que el módulo alcanzaba temperaturas demasiado altas, por lo que se pudo concluir que el tiempo de residencia del fluido era muy pequeño y no extraía eficientemente el calor generado. Por tanto, en este proyecto, se reduce el flujo másico para mejorar el rendimiento respecto al caso anterior. Además, en el estudio anterior los parámetros del modelo eléctrico de la celda considerada no estaban disponibles, así que se utilizaron los parámetros que vienen por defecto en ANSYS Fluent. En este estudio, se utilizan los parámetros eléctricos reales de la batería Toshiba SCiB^{TM} y se analizan las diferencias entre ambos modelos. Finalmente, en un intento de encontrar otra estrategia de refrigeración más eficiente, se propone y se simula un sistema de refrigeración por inmersión, y se estudian las diferencias entre ambos métodos de refrigeración.

Palabras clave: refrigeración indirecta, placa fría, módulo de baterías, Toshiba SCiB^{TM}, descarga, modelo de circuito equivalente, refrigeración por inmersión.

Resum

Durant el desenvolupament d'aquest projecte, es realitza un estudi comparatiu del comportament d'un mòdul de bateries amb refrigeració indirecta per placa freda. La bateria estudiada és una Toshiba SCiB^{TM}. Després d'una introducció sobre les bateries i el seu principi de funcionament, s'inclou una breu discussió sobre els diferents models disponibles en el programa ANSYS Fluent, i s'utilitza el model de circuit equivalent (ECM) per als càlculs. El disseny del mòdul de bateries i del sistema de refrigeració indirecta està basat un estudi previ y es descriu completement ací. En ell s'estudia l'efecte del sistema de refrigeració per a una descàrrega de la bateria de 4C i un flux màssic total de 2.5 kg/s. Els resultats mostren que el mòdul assolia temperatures massa altes, per la qual cosa es va poder concloure que el temps de residència del fluid era molt menut i no extreia eficientment la calor generada. Per tant, en aquest projecte, es redueix el flux màssic per millorar el rendiment respecte al cas anterior. A més, en l'estudi anterior els paràmetres del model elèctric de la bateria considerada no estaven disponibles, així que es van utilitzar els paràmetres que vénen per defecte en ANSYS Fluent. En aquest estudi, s'utilitzen els paràmetres elèctrics reals de la bateria Toshiba SCiB ^{TM} i s'analitzen les diferències entre els dos models. Finalment, en un intent de trobar una altra estratègia de refrigeració més eficient, es proposa i es simula un sistema de refrigeració per immersió, i s'estudien les diferències entre els dos mètodes de refrigeració.

Paraules clau: refrigeració indirecta, placa freda, mòdul de bateries, Toshiba SCiB^{TM}, descàrrega, model de circuit equivalent, refrigeració per immersió.

Contents

List of Figures

List of Tables

List of Symbols

$\dot{m}$ Mass flow

$\dot{Q}_{\text{extracted}}$ Heat extracted by the cooling fluid

$\dot{Q}_{\text{generated}}$ Heat generated by the battery module

$\dot{q}_{abuse}$ Heat generation due to thermal runaway reactions under thermal abuse condition

$\dot{q}_{ECh}$ Electrochemical reaction heat due to electrochemical reactions

$\dot{q}_{short}$ Heat generation rate due to internal short-circuit

μ Dynamic viscosity

ρ Density

σ_+ Effective electric conductivity for the positive electrode

σ_- Effective electric conductivity for the negative electrode

φ_+ Phase potential for the positive electrode

φ_- Phase potential for the negative electrode

A Cross section area

AC Active cooling

C Capacitance

C_p Specific heat at constant pressure

Cf Friction coefficient

D_H Hydraulic diameter

f Friction factor

h Convective heat transfer coefficient

I Electric current

j_{ECh} Volumetric current transfer rate due to electrochemical reactions

j_{short} Volumetric current transfer rate due to internal short-circuit

k Thermal conductivity

L	Length
Nu	Nusselt number
P	Perimeter
Pr	Prandtl number
$Q_{nominal}$	Battery total electric capacity
Q_{ref}	Battery capacity used in experiments
R	Resistance
Re	Reynolds number
soc	State of charge
T	Temperature
t	Time
T_∞	Free stream temperature
U	Open circuit potential of an electrode reaction
u_∞	Free stream velocity
V	Battery cell voltage
V_{OCV}	Open circuit voltage
Vol	Active zone volume of a single battery

List of Abbreviations

12S1P 12 Series 1 Parallel.

AC Active Cooling.

BTMS Battery Thermal Management Systems.

CAD Computer Assisted Design.

CFD Computational Fluid Dynamics.

CMT *Instituto Universitario CMT-Motores Térmicos*.

ECM Equivalent Circuit Model.

EV Electric Vehicles.

HEV Hybrid Electric Vehicles.

HFE Hydrofluoroether.

LTO Lithium Titanate Oxide.

MSMD Multi-Scale Multi-Domain.

NTGK Newman, Tiedemann, Gu and Kim.

OCV Open Circuit Voltage.

P2D Newman Pseudo-2D.

PC Personal Computer.

PEV Pure Electric Vehicles.

PHEV Plug-In Hybrid Electric Vehicles.

SCiB^{TM} Super Charge Ion Battery.

SOC State of Charge.

TUI Text User Interface.

VAT Value Added Tax.

1 Introduction

The science has been crystal clear during the last decades: climate change is a reality and the environment is endangered. This statement has been highly controversial for a long time, but in recent years it seems that the situation has begun to change and the concern about our planet's environment status has started to grow, placing many sectors in a difficult position. Now, the different industries must find cleaner, more sustainable alternatives to the harmful and restricted energy sources that have been utilized thus far.

Transportation is one of the businesses that has been pushed into the limelight, and has started to be regulated by governments throughout the world due to its significant contribution to overall CO_2 emissions. For example, in 2020, over 26% of total energy consumption in the United States was used to move people and goods from one location to another, and petroleum products accounted for around 90% of the total energy use of this sector [1]. However, electricity represented less than 1% of the overall transportation sector energy usage.

As a result, petrol engines have been the subject of growing criticism in recent years and have become the objective of some economic disincentives imposed by many governments. Therefore, the gradual disappearance of petrol engines has started to become a reality, making room for new types of vehicles, namely Hybrid Electric Vehicles (HEV), Plug-In Hybrid Electric Vehicles (PHEV), and Pure Electric Vehicles (PEV). All these vehicles have either a partial or complete electric propulsion system, which is generally powered by a battery pack.

Between all types of batteries that have been used in the past, lithium-ion ones are the most popular kind in recent applications due to their better performance capabilities and efficiency. These have a higher energy density than their equivalents and so take up less space and weight [2]. Moreover, they allow for a longer charging interval only at a slightly greater cost. Also, it could be stated that the most difficult aspect of Li-ion batteries is keeping their temperature under control.

Inside a battery cell, many of the electro-chemical reactions that take place are exothermic [3], which implies that if the heat created in the battery is not effectively managed, the temperature in the battery might grow, resulting in negative consequences such as capacity and power fading, uneven electrical performance [4], and thermal runaway, which could result in considerably more heat production and, eventually, an explosive breakdown [4][5][6].

The employment of Battery Thermal Management Systems (BTMS) is a solution to this problem. There exist multiple types of BTMS, and they may be compared in many ways. A typical approach to categorize them is according to their power consumption [5]: a BTMS might be either active or passive. Passive cooling thermal management systems are designed for low-energy batteries and do not account for any power-consuming devices in order to maintain the temperature of the battery. Some commonly used passive BTMS are natural air cooling, Phase Change Materials (PCM), and heat pipes [7]. Active thermal management, on the other hand, involves the use of an external power supply and temperature-controlling equipment, and is more commonly employed in the automobile sector. Some examples are

forced air [8], liquid cooling [9] [10], and jackets. Another way to classify all the preceding BTMS is as direct or indirect refrigeration systems, depending on whether the battery is in direct contact with the refrigeration fluid or not [11].

Knowing the importance of the use of a BTMS in Li-ion batteries, this project offers a Computational Fluid Dynamics (CFD) study of a cold-plate based refrigeration of a prismatic battery module using ANSYS Fluent. The case of study is a battery module composed by 12 Toshiba Super Charge Ion Battery (SCiB^{TM}) cells in series. The design of the battery module and the indirect refrigeration system is based on a previous study made by A. Arcila [12], in which the effect of the refrigeration system on the module temperature was studied for a 4C discharge and an overall 2.5 Kg/s inlet mass flow. In said work, it is shown that the module attained too high temperatures, and it was concluded that the residence time of the fluid was too small to efficiently extract the heat generated.

Therefore, the objective of this project is to extend this previous study. In the first place, the validity of the previous conclusion will be assessed, by simulating the case with a reduced mass flow. To do so, the mesh of the battery module and refrigeration system were provided by *Instituto Universitario CMT-Motores Térmicos* (CMT). In the aforementioned study, the real parameters of the Toshiba SCiB^{TM} cell were not available, so the default ones in ANSYS Fluent were used. Now, a complete analysis will be done using the real electrical parameters of the Toshiba SCiB^{TM}, since they are now available and again provided by CMT, and the results from both battery models will be compared. Finally, as an attempt to find another more efficient BTMS for the considered battery module, an immersion based refrigeration system is proposed and simulated, and the differences between both liquid cooling refrigeration methods will be studied.

2 Batteries

Batteries are a widely used source of electrical energy all over the world. From mobile phones, to laptops or even cars, they offer portable power in a relatively simple manner.

In general terms, a battery is composed by a basic power unit called the *cell*, two *electrodes* and a chemical inside these electrodes known as *electrolyte* [13], as seen in Figure 1. These elements are usually inside a metal or plastic outer case in order to ensure safety. It is important to mention that both electrodes are always formed by different materials, which need to be conductors of electricity. This difference ensures that the current flows in the form of electrons, which will be given up by one electrode and captured by the other. Also, a battery is formed by the combination of two or more cells.

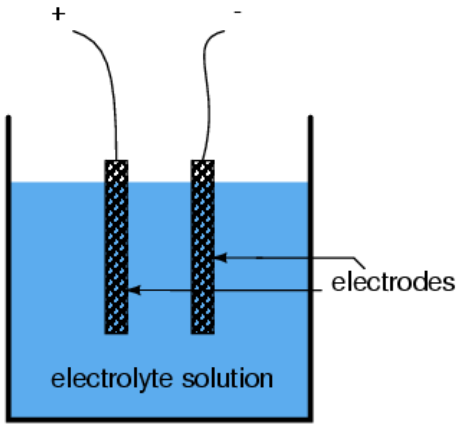

Figure 1: Voltaic cell elements [14]

Now, it is important to explain how does a battery generate electrical energy. The battery includes a positive terminal, which is connected to the positive electrode and is called the *cathode*, and a negative terminal or *anode*, connected to the negative electrode. When the battery starts discharging, two separate chemical reactions occur. On the one hand, electrons are given away by the negative electrode, causing positive ions to form. These positive ions flow into the electrolyte, whilst the electrons enter an outside circuit towards the positive electrode, thus being an electric current. On the other hand, at the positive electrode, incoming electrons recombine with the ions from the electrolyte. This process can be graphically seen in Figure 2. It is also important to take into account that the specific chemical reactions occurring inside the battery will depend on the materials that form the electrodes and the electrolyte. Finally, when the chemicals have been completely depleted and no more positive ions can be formed, the battery is considered completely discharged.

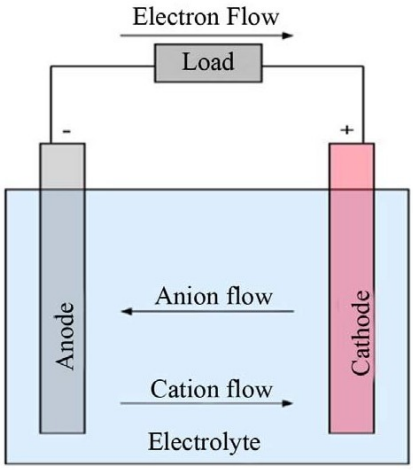

Figure 2: Working principle of a battery [13]

As for the different types of batteries, a common classification divides them into primary and secondary ones. Primary batteries are disposable and cannot be recharged, whilst secondary ones can. Recharging a battery can be done by passing a current through it in the opposite direction than for the discharge process.

Primary batteries present one advantage against secondary ones, as they can store more energy and last longer than a rechargeable one with the same size. However, as it has been previously mentioned, they cannot be recharged, so they can be considered to pollute the environment to a higher extent. The three main types of primary batteries are the zinc carbon, alkaline and lithium ones.

Secondary batteries, also referred to as rechargeables, became common when mobile power sources started being needed. In this work, the **lithium-ion secondary battery** will be used (not to be confused with the lithium primary battery), due to its material properties, such as specific energy and power, cycle life, and nominal voltage. They are naturally lightweight batteries that can store a great amount of energy in its atomic bonds [15]. These characteristics have made lithium-ion batteries widely used amongst many manufacturers for Electric Vehicles (EV) applications.

In a Li-ion battery, the anode is generally made of a carbon material. Its low working potential makes graphite the most popular solution [16], however, other anodes are made of titanium compounds or silicon based materials, for example.

As for the cathode, it needs to be made of a material which contains lithium, such as a layered oxide, a spinel or a polyanion. The most commonly used one is the cobalt-based layered oxide $LiCoO_2$. This material is chosen because of the numerous advantages it offers, such as its high energy density and good cyclic performance. However, its high price and low thermal stability are nowadays leading to the use of different compounds like the iron-based polyanions $LiFePO_4$, which constitute a cheaper alternative to the previusly mentioned material [17].

In a Li-ion battery, lithium ions (Li^+) flow between the two electrodes, as shown in Figure 3.

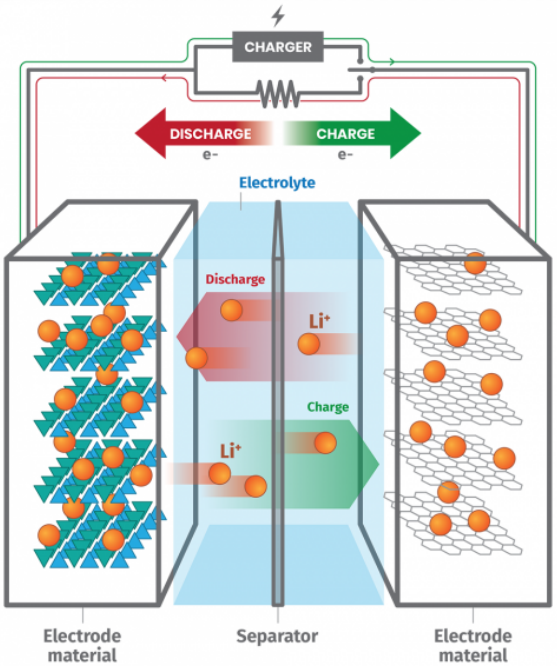

Figure 3: Li-ion battery working principle illustration [18]

As for the electrolyte, liquid solutions are commonly lithium salts, being hexafluorophosphate ($LiPF_6$) the most popular one, dissolved in organic solvents [20]. Nowadays, solid electrolytes are also being investigated as they would reduce the risk of electrolyte leaks. The most researched ones are ceramic materials, especially lithium metal oxides.

Another element present in Li-ion batteries is the separator, which is located in between both electrodes and can be easily located in Figure 3. It is a permeable membrane that separates the anode and the cathode in order to prevent electrical short circuits, whilst still allowing lithium ions to travel. Examples of materials that can be used in separators are ethylene, polyethylene or polypropylene.

Now, Table 1 illustrates the large differences that can exist amongst the different types of lithium-ion batteries. It must be pointed out that the high safety and life cycle of the Lithium Titanate Oxide (LTO) battery makes it very popular amongst various automobile applications.

Chemistry	**Lithium Cobalt Oxide**	**Lithium Manganese Oxide**	**Lithium Titanate Oxide**
Abbreviation	LCO	LMO	LTO
Nominal voltage [V]	3.60	3.70	2.40
Specific Energy [Wh/kg]	150–200	100–150	70–80
Typical Cycle life	500–1000	300–700	3000–7000
Packaging types	18650, prismatic and pouch cell	Prismatic	Prismatic
Applications	Phones, tablets, laptops	Power tools, medical devices, powertrains	EV, solar street lighting
Comments	High energy, limited power	High power, less capacity; safer than Li-cobalt	Long life, fast charge, wide temperature range and safe. Low capacity, expensive

Table 1: Summary of common Li-ion batteries. Adapted from [19]

2.1 Toshiba SCiB^{TM} Battery

In this project, the employed battery will be the Toshiba SCiB^{TM}. It is a LTO rechargeable battery which can be charged up to 90% of its capacity in 10 minutes. Amongst its most relevant characteristics [21], the following can be found:

- Low risk of fire or explosion due to the reduced probability of overheating.
- A lifespan of around 20,000 cycles and a low capacity degradation.
- As it has been previously mentioned, a rapid charging, which does not cause a significant capacity degradation.
- A high current charge and discharge, which allows a high power input/output in a short time span. This makes it possible to efficiently store the braking energy of a vehicle, and also starting the motor without the presence of any external aid.
- The possibility of establishing working temperatures as low as -30°C, due to the fact that lithium metal does not precipitate at these temperatures.
- A wide State of Charge (SOC) effective range from 0% to 100% and good input/output characteristics. This allows mounting less battery cells in a system.

An example of a Toshiba SCiB^{TM} cell can be seen in Figure 4.

Figure 4: Toshiba SCiB^{TM} cell [22]

It is also interesting to mention that this type of batteries has been widely implemented. For example, they are used in a prototype laptop made by Toshiba and the Schwinn Tailwind and Honda's EV-neo electric bikes. As for its employment in automobile applications, this battery fuels the Japanese version of Mitsubishi's i-MiEV and Minicab MiEV and in Honda's Fit EV.

Finally, the geometric dimensions of this battery cell are shown in Figure 5.

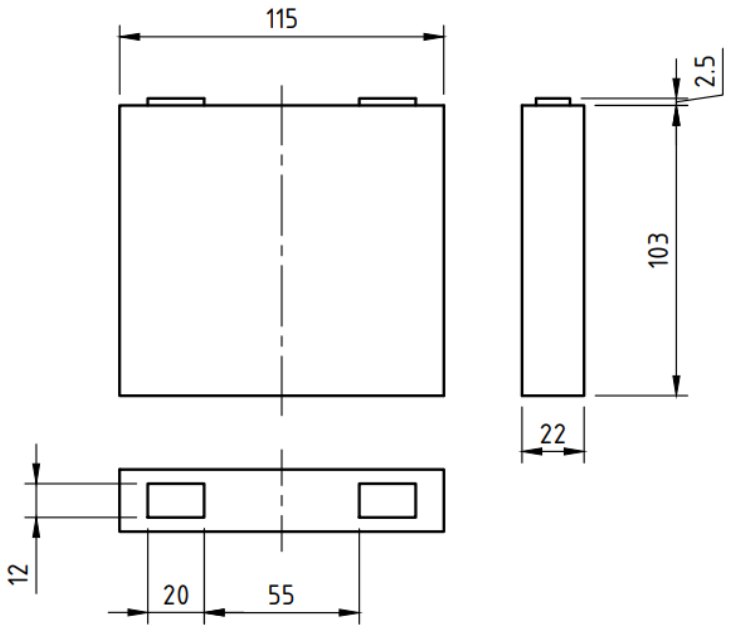

Figure 5: Toshiba SCiB^{TM} cell dimensions in mm

2.2 Battery Modelling

Modelling a battery is a complex process that depends on the number of parameters to be introduced, such as ageing or charge and discharge differences. Moreover, several scales can be taken into account, from the microscopic point of view of the ion diffusion to a whole pack.

For the completion of this thesis, the software ANSYS 2019 R2 has been used, more specifically, the CFD Fluent solver. For characterising a battery's behavior in ANSYS Fluent, the following solution methods can be employed:

- CHT coupling method
- FMU-CHT coupling method
- Circuit Network solution method
- MSMD solution method

In this project, the **Multi-Scale Multi-Domain (MSMD) solution method** will be used, as it can be applied for systems with diverse physical properties and a complex geometry.

This solution method makes use of the following equations for solving the thermal and electrical fields. Equation 1 represents an energy equation, and Equation 2 shows the potential equations, which only need to be solved in the active zones of the cell, that is, the locations where electro-chemical reactions occur.

$$\frac{\partial \rho C_p T}{\partial t} - \nabla \cdot (k \nabla T) = \sigma_+ \mid \nabla \phi_+ \mid^2 + \sigma_- \mid \nabla \phi_- \mid^2 + \dot{q}_{ECh} + \dot{q}_{short} + \dot{q}_{abuse} \tag{1}$$

$$\begin{aligned} \nabla \cdot (\sigma_+ \nabla \varphi_+) &= -(j_{ECh} - j_{short}) \\ \nabla \cdot (\sigma_- \nabla \varphi_-) &= j_{ECh} - j_{short} \end{aligned} \tag{2}$$

This solution method allows using a diversity of electro-chemical models, which are the following:

- Newman, Tiedemann, Gu and Kim (NTGK) model [23]
- Equivalent Circuit Model (ECM) [24]
- Newman Pseudo-2D (P2D) model [25]

2.2.1 NTGK model

Proposed by reference [23], this is a model based on semi-empirical results, which offers satisfactory solutions when working with steady electrical loads. However, if sudden alterations occur in the electric load, this model fails to take into account inertial changes. Therefore, other models such as the ECM one will be more accurate.

2.2.2 Equivalent Circuit Model (ECM)

In this semi-empirical model, an electrical circuit is used for simulating the electrical behavior of the battery. As in the work of Chen [24], ANSYS Fluent employs a second order ECM. This model makes use of six different parameters: an Open Circuit Voltage (OCV), three resistors and two capacitors, all of them being a function of the SOC. Figure 6 shows a graphical scheme of the model.

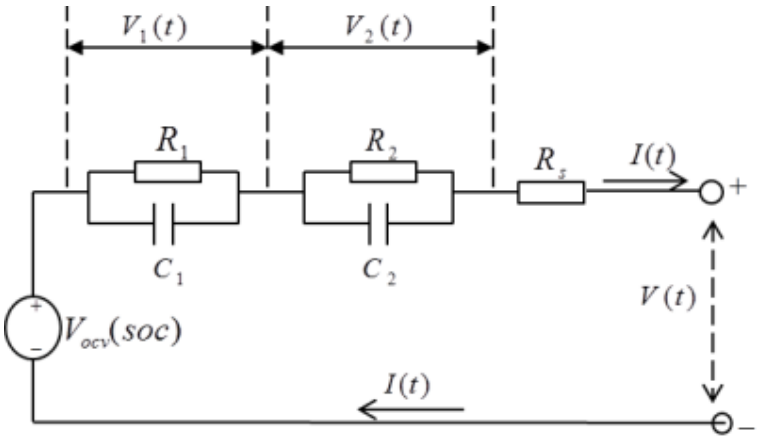

Figure 6: ECM scheme [26]

The relation between voltage and current can be obtained by solving the electrical circuit equations:

$$
\begin{aligned}
V &= V_{OCV}(soc) - V_1 - V_2 - R_S(soc)I(t) \\
\frac{dV_1}{dt} &= -\frac{1}{R_1(soc)C_1(soc)}V_1 - \frac{1}{C_1(soc)}I(t) \\
\frac{dV_2}{dt} &= -\frac{1}{R_2(soc)C_2(soc)}V_2 - \frac{1}{C_2(soc)}I(t) \\
\frac{d(soc)}{dt} &= \frac{I(t)}{3600Q_{ref}}
\end{aligned}
\tag{3}
$$

Also, ANSYS Fluent allows calculating the six parameters (the OCV, the three resistors and both capacitors) in three different ways:

1. Expressing them as fifth order polynomials as a function of the SOC

$$\begin{aligned} R_S &= a_0 + a_1(soc) + a_2(soc)^2 + a_3(soc)^3 + a_4(soc)^4 + a_5(soc)^5 \\ R_1 &= b_0 + b_1(soc) + b_2(soc)^2 + b_3(soc)^3 + b_4(soc)^4 + b_5(soc)^5 \\ C_1 &= c_0 + c_1(soc) + c_2(soc)^2 + c_3(soc)^3 + c_4(soc)^4 + c_5(soc)^5 \\ R_2 &= d_0 + d_1(soc) + d_2(soc)^2 + d_3(soc)^3 + d_4(soc)^4 + d_5(soc)^5 \\ C_2 &= e_0 + e_1(soc) + e_2(soc)^2 + e_3(soc)^3 + e_4(soc)^4 + e_5(soc)^5 \\ V_{OCV} &= f_0 + f_1(soc) + f_2(soc)^2 + f_3(soc)^3 + f_4(soc)^4 + f_5(soc)^5 \end{aligned} \tag{4}$$

2. By using a function proposed by Chen [24]

$$\begin{aligned} R_S &= a_0 + a_1 exp[-a_2(soc)] \\ R_1 &= b_0 + b_1 exp[-b_2(soc)] \\ C_1 &= c_0 + c_1 exp[-c_2(soc)] \\ R_2 &= d_0 + d_1 exp[-d_2(soc)] \\ C_2 &= e_0 + e_1 exp[-e_2(soc)] \\ V_{OCV} &= f_0 + f_1(soc) + f_2(soc)^2 + f_3(soc)^3 + f_4 exp[-f_5(soc)] \end{aligned} \tag{5}$$

3. By means of a 2D table that expresses each parameter as a function of the SOC and the temperature. It is important to notice that this is the only method that takes into account the temperature effect.

Finally, the ECM calculates the source terms as follows:

$$j_{ECh} = I\frac{Q_{Nominal}}{Q_{ref}Vol} \tag{6}$$

$$\dot{q}_{ECh} = j_{ECh}\Big[V_{OCV} - (\phi_+ - \phi_-) - T\frac{dU}{dT}\Big] \tag{7}$$

The described model offers successful results for complex simulations and does not compromise the computational cost, being fairly cheap regarding this aspect. It is also a very versatile model, as it cannot only be used for modelling Li-ion batteries but also other types of solid ones, whilst the other two models can only be employed when working with lithium based batteries.

2.2.3 Newman's Pseudo-2D model

This last model is by far the one that requires a higher computational cost. It consists in a physics-based model, which is founded on a porous electrode and on concentrated solution theories [25]. This possibility allows modelling the trajectory of the ions across the different layers of the battery.

For this case, it is important to distinguish between two regions: a continuous electrolyte solution, which covers the electrodes and the separator between them, and a solid phase represented as a matrix of regular spheres, which can be found in both electrodes. These regions can be observed in Figure 7.

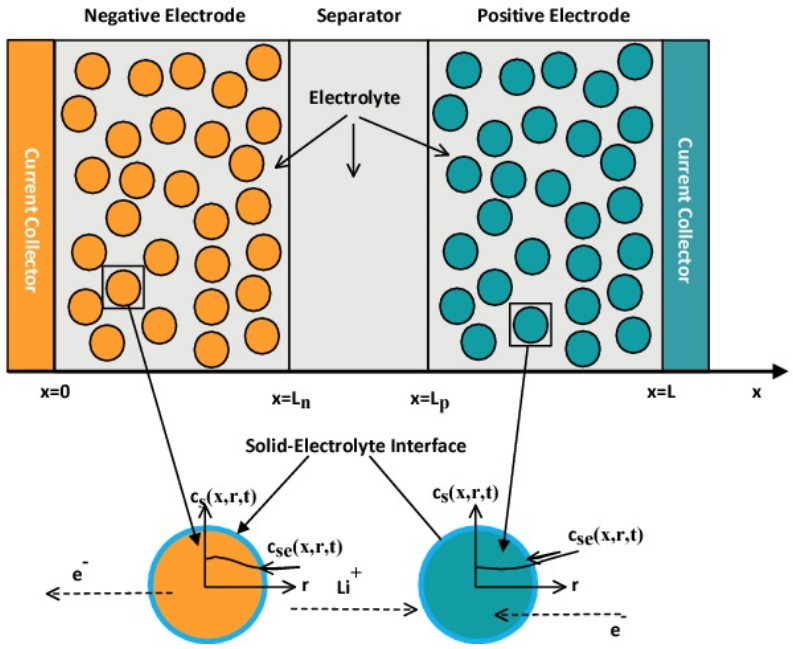

Figure 7: P2D model schematics, adapted from [27]

During discharge, lithium ions and electrons are diffused radially by the negative electrode solid particles, from the center to the surface. The ion then travels to the positive electrode by diffusion, and it is later stored inside the positive electrode spheres, causing an increase in concentration.

Finally, for mathematically expressing these phenomena, the charge and mass concentration laws are used.

3 Methodology

In this section, the design of the battery module, refrigeration systems and electrical models for the cell used will be fully described. The different cases that are going to be calculated will be explained, including their geometry, mesh and simulation setup.

3.1 Battery Module Design

Based on the chosen battery cell mentioned in Section 2.1, the design proposed is a compact 12 cells battery module, which are connected in series using thin rectangular bus-bars, building a 12 Series 1 Parallel (12S1P) battery module (Figure 8a). The module has a casing where the batteries are located, which can be seen in Figure 8b. The casing walls thickness is 2 mm and there is a 1 mm gap between the cells and the casing, and between the faces of the cells. There are also 5 mm high spacers at the bottom of the casing that help to battery to pack into place (Figure 9).

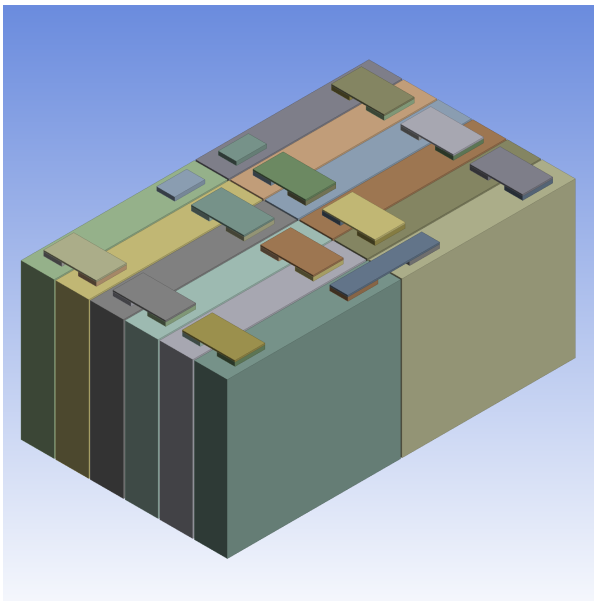

(a) Module without casing

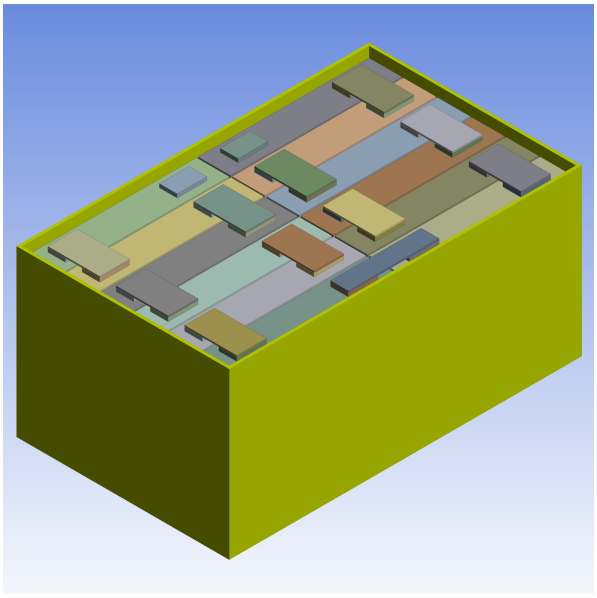

(b) Module with casing

Figure 8: Isometric view of the battery module

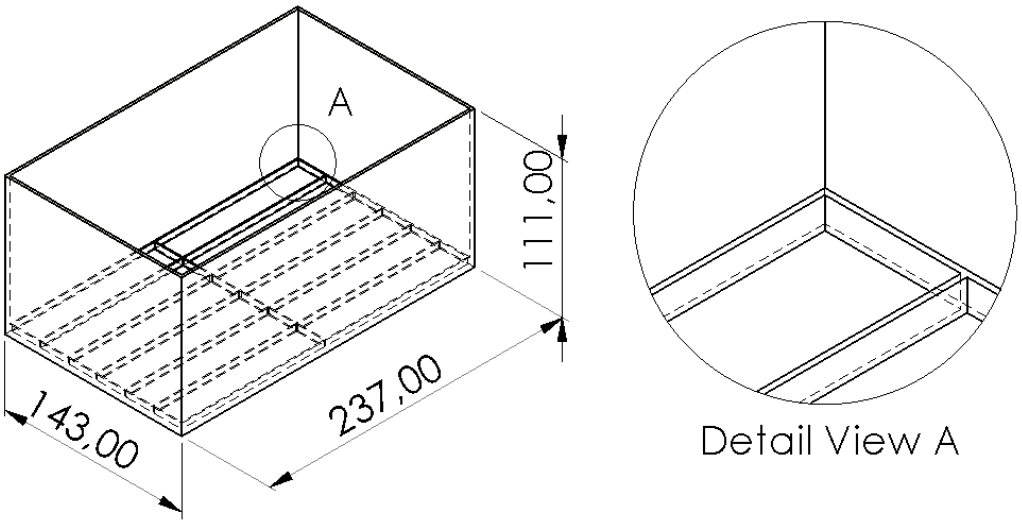

Figure 9: Main measurements and details of the module casing in mm [12]

3.2 Electro-Thermal Model

After defining the battery module, the first step will be to study its electro-thermal behavior. For this project, the ECM described in Section 2.2 is considered, and two different models are used. In order to be able to compare the obtained results with reference [12], the first model corresponds to the ANSYS Fluent default one, as it was the one used in that project. This model belongs to a 850-mAh TCL PL-383562 polymer lithium-ion battery. Its electrical characteristics and ECM coefficients are included in Table 2 and Table 3.

The second model corresponds to the real Toshiba SCiB^{TM}, which electrical characteristics are included in Table 4. The information of the ECM parameters has been provided internally by the CMT in the form of tables. A total of six tables were provided: three for the resistances R_S, R_1 and R_2; two for the capacitances C_1 and C_2; and one for the voltage V_{OCV}. The values of the parameters presented in the tables are a function of the SOC and the temperature. The values can be introduced to ANSYS Fluent with a .tab file. These tables are included in Appendix A.

Chemistry	Polymer Lithium Ion
Nominal voltage [V]	3.7
Discharge cut-off voltage [V]	3.0
Nominal capacity [mAh]	850
Maximum discharge current [A]	1.7(2C)
Discharge operating temperature [°C]	from -20 to +45

Table 2: Main electrical parameters of the ANSYS default battery model [28]

Coefficient	Value	Coefficient	Value
a_0	0.07446	d_2	155.2
a_1	0.1562	e_0	4475
a_2	24.37	e_1	-6056
b_0	0.04669	e_2	27.12
b_1	0.3208	f_0	3.685
b_2	29.14	f_1	0.2156
c_0	703.6	f_2	-0.1178
c_1	-752.9	f_3	0.3201
c_2	13.51	f_4	-1.031
d_0	0.04984	f_5	35
d_1	6.603		

Table 3: ECM coefficients of the ANSYS default battery [28]

Chemistry	Lithium Titanium Oxide
Nominal voltage [V]	2.3
Discharge cut-off voltage [V]	1.5
Nominal capacity [Ah]	23
Discharge operating temperature [°C]	from -30 to +45

Table 4: Main electrical parameters of the Toshiba SCiB^{TM} model [21]

3.3 Non-refrigerated Battery Module

3.3.1 Geometry

The geometry that will be used to study the two electro-thermal models is the one described in Section 3.1, which corresponds to the 12S1P battery module with casing. One key aspect is to give a specific name to all bodies and surfaces so that it is possible to assign certain characteristics later in the setup (boundary conditions, materials, etc.).

The battery module consists in total of 48 bodies (Figure 10):

- 12 cells
- 12 positive tab zones
- 12 negative tab zones
- 11 busbars
- 1 casing

Additionally, 2 surfaces must be named, that will act as surfaces for boundary conditions for the electrical model (Figure 10):

- Tab_P
- Tab_N

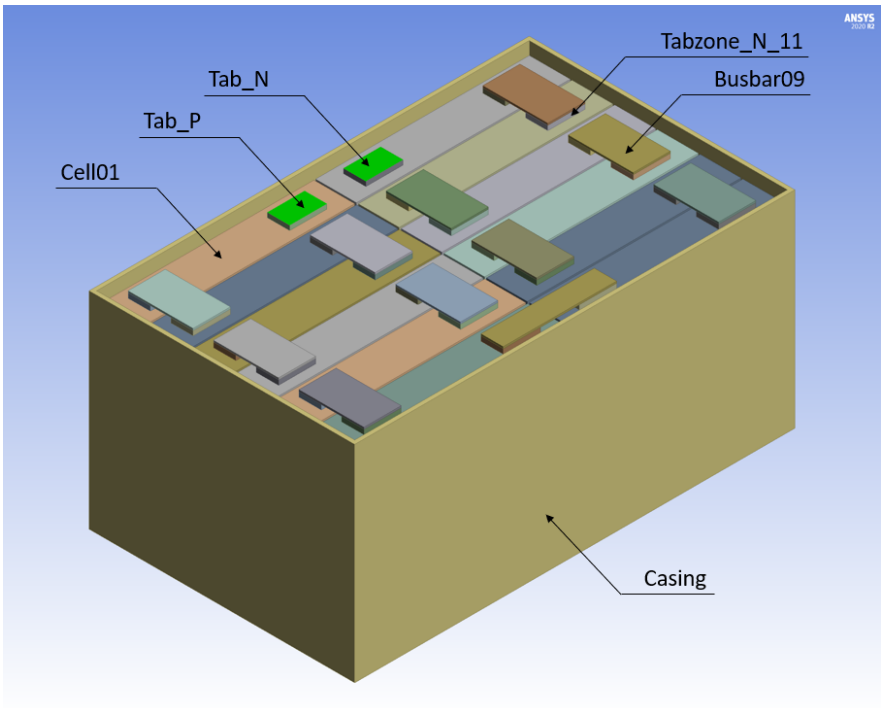

Figure 10: Isometric view of the non-refrigerated battery module with named selections

It is very important to mention that all the bodies have been grouped as a single part. This guaranteed that the interfaces between bodies would allow a conforming mesh when the mesh was generated, ensuring a correct calculation of the heat transfer across the bodies.

3.3.2 Mesh

The mesh used to evaluate the thermo-electrical behavior of the battery model provided by the CMT is the one used in [12], and it will be described next. The mesh was generated using the "body sizing" tool in ANSYS, so that different maximum sizes for the elements of the mesh could be assigned to different bodies, and therefore to be able to provide enough definition to properly calculate the physics phenomena occurring in the battery module. A mesh independence study was made in [12]. The resulting mesh is made of 3.2 million elements. A summary of the body sizing can be found in Table 5. In Figure 11 a cross-section of the mesh is shown, where a section of a tab, busbar, cell, and casing can be seen.

Bodies	**Element size [m]**	**Element type**
Tabzones and busbars	$5 \cdot 10^{-4}$	Hexahedrons
Cells	$4 \cdot 10^{-3}$	Tetrahedrons
Casing	$1 \cdot 10^{-3}$	

Table 5: Body sizing of the battery module mesh

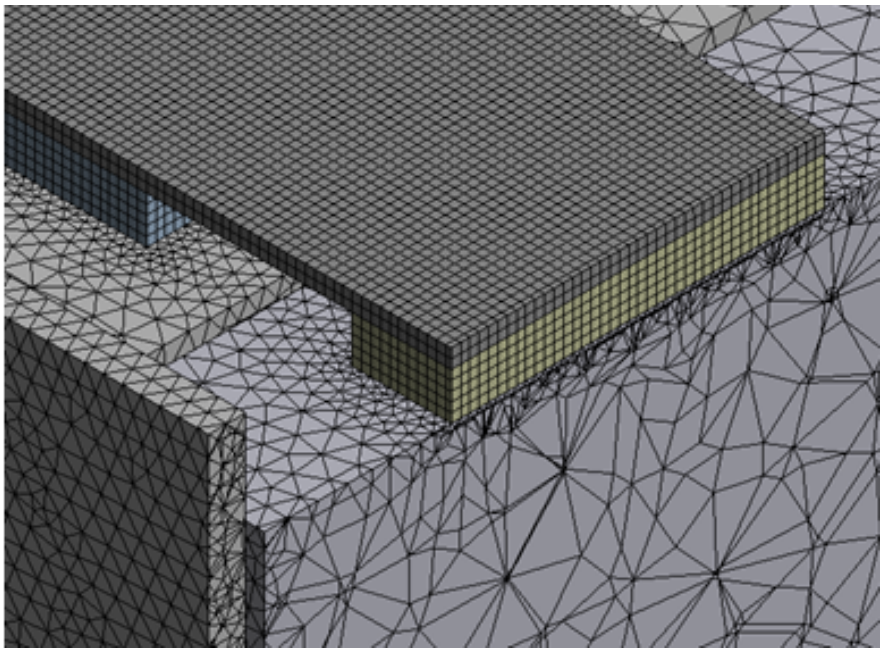

Figure 11: Cross-section of the battery module mesh [12]

3.3.3 Model Setup

Before starting with the setup, the mesh needs to be loaded into ANSYS Fluent. Once it has been imported, a regular battery model setup is done, following the instructions that can be found in the ANSYS Tutorial Guide [26] step-by-step.

The first step is to define the solver options. The simulation is set as a **transient** case. The **energy equation** is **enabled** and the **flow and turbulence** equations are **disabled**, since in this case there is no need to calculate any fluid flow.

The next step is to load to Fluent the **Dual-Potential MSMD battery model** add-on, using the Text User Interface (TUI). For the E-chemistry model the ECM is set. The Joule heat in active zones is enabled and the specified C-rate option is selected. The C-rate will be constant along the simulation, with a value of 4.

Two different simulations will be carried out using the two different electro-thermal models described in Section 3.2. The discharging parameters of each model are introduced. In the case of the ANSYS default battery model, the parameters in Table 3 are introduced manually.

In the case of the Toshiba SCiB^{TM} model, the different data tables are introduced with .tab files.

As for the **conductive zones conditions**, all cells are defined as active zones, and the busbars and tab zones as passive. The surfaces Tab_P and Tab_N are defined as the external connectors.

Now, the **materials** definition will be covered. 3 different solid materials are used. For the casing, aluminum is used. For the cells material (e_material), and the tabs and busbars material (busbar_material), the correlations proposed in the ANSYS Tutorial Guide [26] are used, using the material properties from [29] and [30]. A summary of the material properties can be found in Table 6.

Property	**Aluminum**	**e_material**	**busbar_material**
ρ [kg/m^3]	2719	2092	2719
C_p [J/(kg K)]	871	678	871
k [W/(m K)]	202.4	18.2	20
σ [S/m]	$3.541 \cdot 10^7$	$3.541 \cdot 10^7$	$3.541 \cdot 10^7$

Table 6: Material properties of the battery module

Regarding the **boundary conditions** definition, all the contact surfaces between the different bodies are established as a thermally coupled wall. In the case of the surfaces that are exposed to the "air" (except for the external connectors Tab_P and Tab_N), a thermal condition of convection is applied. A natural convection of the air is considered, with a free stream temperature T_∞ of 300 K and a heat transfer coefficient h of 5 W/(m^2·K).

Next, the solution controls are specified. The battery module itself enforces a **stopping condition** when the cut-off voltage is reached, therefore all convergence criteria are deactivated.

Afterwards, 4 **report** definitions are created to extract information for the analysis of the results in Section 4. The reports are the following:

- SOC
- Voltage
- Maximum temperature of the module
- Total heat generation of the module

Eventually, the model is initialized. As recommended by references [12], the time step has been established to be 0.1 seconds, with 25 iterations per time step.

3.4 Cold-plate Refrigeration System Design

The refrigeration system used to refrigerate the module described in Section 3.1 was designed based on the Audi e-tron cooling system [31], so that it resembles a realistic refrigeration system. The dimensions of the inlet and outlet collectors and the general configuration have been modified to adapt it to refrigerate the battery module considered in order to obtain a satisfactory distribution of the fluid across all channels.

The geometry of the refrigeration system used can be appreciated in Figure 12. It consists of two 55 mm diameter cylindrical collectors (inlet and outlet) and 6 plates with 28 micro-channels (168 channels) which connect both collectors in a U-shaped layout. Each micro-channel measures 2x5x530 mm and are separated between them by a distance of only 0.5 mm. The distance between two plates is 83.5 mm and the total length of the inlet and outlet collectors is 1428 mm.

A total of 12 battery modules will sit on top of the refrigeration system, which means that each plate will refrigerate two battery modules. The grey rectangles in Figure 12a represent each of the modules laying on each plate.

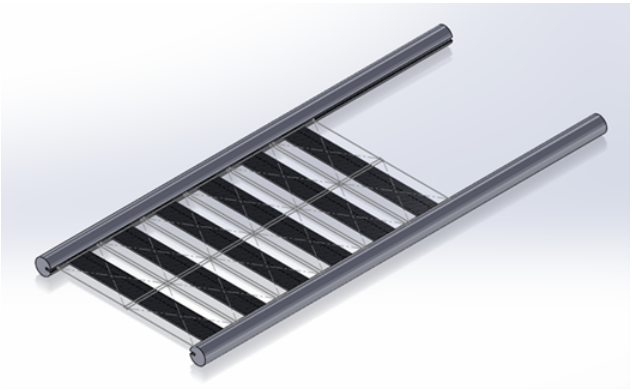

(a) Isometric view of the refrigeration system

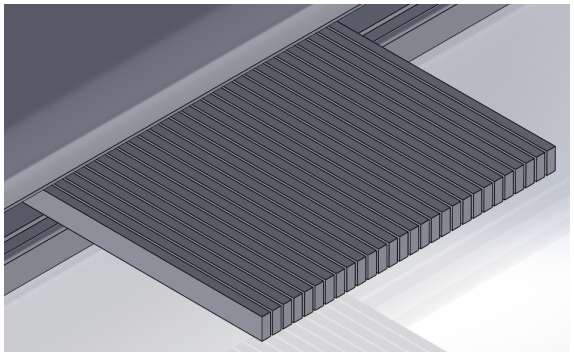

(b) Detailed view of a plate and the outlet collector

Figure 12: Geometry of the refrigeration system [12]

As proven by references, this refrigeration system design ensures equal cooling for all cells. A study performed by A. Arcila [12] confirms that for mass flow values between 0.5 kg/s and 2.5 kg/s the speed across all plates is almost identical, since the velocity distribution variation is less than 5.1%. Therefore, the coolant is uniformly distributed between all micro-channels, and the refrigeration of the 12 battery modules will not have significant differences. Hence, in order to save a considerable amount of computational cost, it is enough to consider the refrigeration of a single battery module.

3.5 Cold-plate Refrigerated Battery Module

Once the battery module in Section 3.1 and refrigeration system in Section 3.4 are designed, both models are coupled together into a single simulation, so that the efficiency of the cold-plate based refrigeration system can be studied regarding the thermal management of the module.

3.5.1 Geometry

The geometry that will be used to study the behavior of the refrigerated battery module is very similar to the one used in Section 3.3.1 but adding a plate of the refrigeration system (28 channels) under a single battery module lengthwise. As in Section 3.3.1, a specific name is given to all the new bodies and surfaces added.

In this case, the refrigerated battery module consists in total of 77 bodies, after adding the following 29 bodies (Figure 13):

- 1 refrigeration body
- 28 fluid channels

Also, 2 additional groups of surfaces are named, that will act as surfaces for boundary conditions for the fluid (Figure 13):

- Inlet
- Outlet

3.5.2 Mesh

The mesh used to evaluate the behavior of the refrigerated battery model was again provided by the CMT and is the one used in [12]. The mesh was generated using one more time the "body sizing" tool in ANSYS, but also using the "edge sizing" tool. In this mesh, the edge sizing was used in each fluid channel to define the total number of elements along two edges: the horizontal and vertical edges of the section of the channels. The horizontal ones were divided in 4 equal parts and the vertical ones were divided in 15 non-equal parts. The segments closer to the top part are smaller in order to capture the boundary layer (Figure 14a). This sections were extruded from the inlet to the outlet faces, creating the mesh appreciated in Figure 14b.

This mesh was also subjected to a mesh independence process until an independent mesh of 4 million elements was obtained. Regarding the body sizing of the different bodies, all element sizes remain the same as in Table 5, but adding the plate (refrigeration body), which elements are hexahedrons with a size of 10^{-3} m.

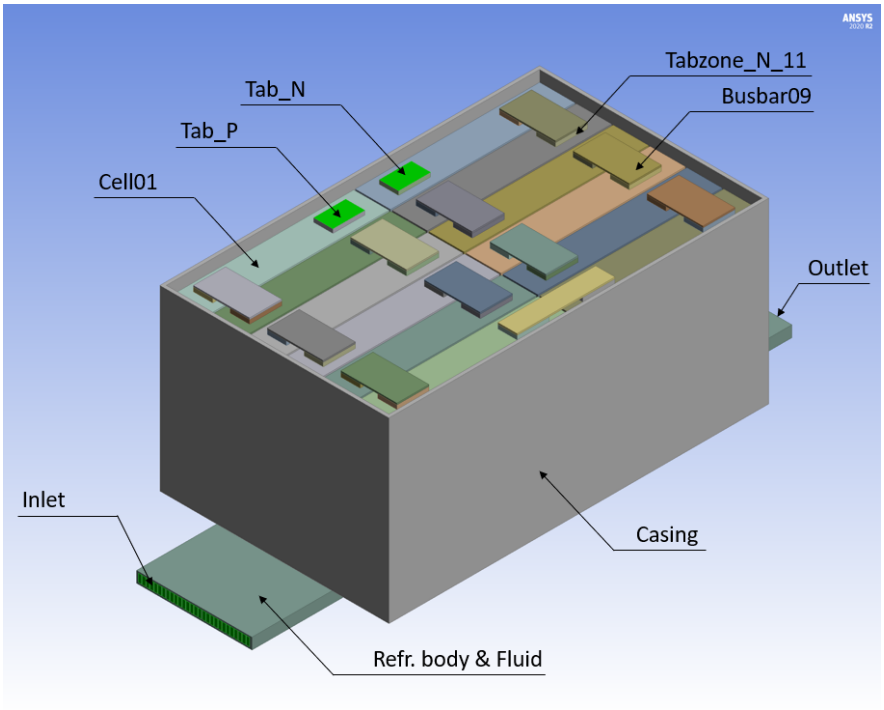

Figure 13: Isometric view of the refrigerated battery module with named selections

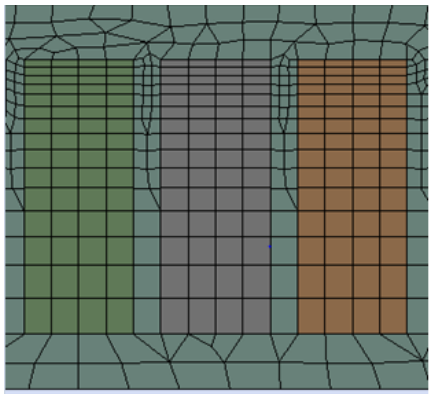

(a) Front view of the channels inlet face

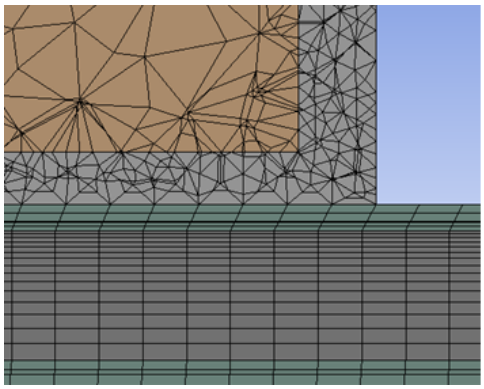

(b) Cross-section view of the mesh

Figure 14: Refrigerated battery module mesh [12]

3.5.3 Model Setup

The setup of this model is similar to the setup made in Section 3.3.3, but some differences are appreciated due to the presence of the refrigeration system, which will be described next.

Regarding the solver options, the solver employed is **pressure-based**. In this simulation, the **flow and turbulence** equations are **enabled**, as there is a fluid (water) flowing through the refrigeration system. Also, it is necessary to define the **viscous model** employed in the simulation. The model selected is a realizable **k-epsilon** with enhanced wall function.

With respect to the **boundary conditions**, an inlet velocity is imposed in the inlet group of surfaces. First, the velocity imposed will be of 1.47 m/s. This value is equivalent to an inlet mass flow of 2.5 kg/s, as is the one used by A. Arcila in his study [12]. Additionally, a velocity of 0.735 m/s will be imposed, which is half the velocity of the previous one (inlet mass flow of 1.25 kg/s). This is made to study if the fluid can extract more heat from the battery module when the residence time is increased.

Additionally, 4 more **report** definitions are created, with the purpose of extracting information about the performance of the refrigeration system. These are:

- Heat flux from the casing to the refrigeration body
- Heat flux from the refrigeration body to the fluid
- Maximum temperature of the fluid at the outlet
- Average temperature of the fluid at the outlet

3.6 Immersion Refrigerated Battery Module

As an additional study, an immersion based refrigeration system is proposed. This system consists on submerging the battery module in direct contact with a dielectric fluid. The fluid will be contained inside the module casing, and will continuously enter and exit the casing through some openings in the casing to avoid the heating of the fluid. All cells are directly exposed to the dielectric coolant to 95% of their height (5 mm of the cells are packed into the casing spacers).

As recommended by references [32], the dielectric fluid used for this study is a Hydrofluoroether (HFE) from 3M^{TM} called NOVEC^{TM} 7500, which is commercially available [33]. Hydrofluoroethers are a type of fluorocarbon dielectric fluids which have many advantages in industrial cooling applications, such as high thermal and chemical stability, immunity to flammability issues, wide range of boiling points and less environmental concerns with respect to other dielectric fluids [34]. In Table 7, the material properties of the dielectric coolant are presented.

Property	**3M^{TM} NOVEC^{TM} 7500**
ρ [kg/m^3]	$-2.0845\ T[°C] + 1665.8;\ 20°C \leq T \leq 70°C$
μ [kg/(m·s)]	$1 \cdot 10^{-7}\ T^2[°C] - 3 \cdot 10^{-5}\ T[°C] + 0.0018;\ 20°C \leq T \leq 70°C$
C_p [J/(kg·K)]	$1.4982\ T[°C] + 1091;\ 20°C \leq T \leq 70°C$
k [W/(m·K)]	$4 \cdot 10^{-7}\ T^2[°C] - 2 \cdot 10^{-4}\ T[°C] + 0.069;\ 20°C \leq T \leq 70°C$

Table 7: Material properties of the dielectric coolant depending on temperature [32] [33]

To simulate the behavior of the immersion refrigeration system in a precise way, a new mesh must be created. The new mesh must include the new design of the inlet, outlet and casing, and the whole volume inside the casing must be meshed, as this is the space in which the fluid will be contained. However, this work is out of the scope of this project, since only an initial approximation of this problem is wanted to be obtained.

Consequently, the mesh used in Section 3.3.2 is going to be employed. The setup for this simulation is identical to the one made for the non-refrigerated battery module. But, to simulate the behavior of the dielectric coolant flowing around the cells, a different thermal condition of convection is applied on the faces in contact with the cooling fluid by changing the value of the convective heat transfer coefficient h.

3.6.1 Determination of h

First of all, some dimensionless numbers must be defined. These dimensionless numbers will be very useful in the calculation of the convective heat transfer coefficient h.

The first one is the Reynolds number, which relates the inertia forces and the viscous forces acting within a fluid. It also allows to predict if the fluid flow is laminar or turbulent.

$$Re = \frac{\rho\ u_\infty\ L}{\mu} \tag{8}$$

The second one is the Prandtl number, which relates the momentum diffusivity and the thermal diffusivity.

$$Pr = \frac{\mu\ C_p}{k} \tag{9}$$

And the last one is the Nusselt number, which is the ratio of the convective and conductive heat transfer at a boundary of a fluid. It is directly related to the convective heat transfer coefficient h.

$$Nu = \frac{h\ L}{k} \tag{10}$$

After these previous definitions, the conditions of the dielectric fluid will be determined. The free stream temperature of the fluid T_∞ is determined to be 300 K, as this was the temperature of the air for the natural convection considered in the previous simulations. The initial temperature of the cells and casing is also considered to be 300 K. Once the free stream temperature is known, the equations in Table 7 are applied. Additionally, using Equation 9, the value of the Prandtl number for the NOVEC^{TM} 7500 is calculated. The values obtained are presented in Table 8.

Property	**3M^{TM} NOVEC^{TM} 7500**
ρ [kg/m^3]	1609.831
μ [kg/(m·s)]	$1.067 \cdot 10^{-3}$
C_p [J/(kg·K)]	1131.267
k [W/(m·K)]	0.0639
Pr [-]	18.877

Table 8: Material properties of the dielectric coolant at $T_\infty = 300$ K

The problem is going to be considered as a convective heat transfer problem in an internal flow. The flow is considered internal because it is flowing in a small gap of 1 mm between the cells, and between the cells and the casing. Therefore, the flow will behave in the same way as a fluid flowing inside a pipe, in which the boundary layer grows from the entrance of the pipe (entrance zone) until covering the whole section (developed flow zone) (Figure 15).

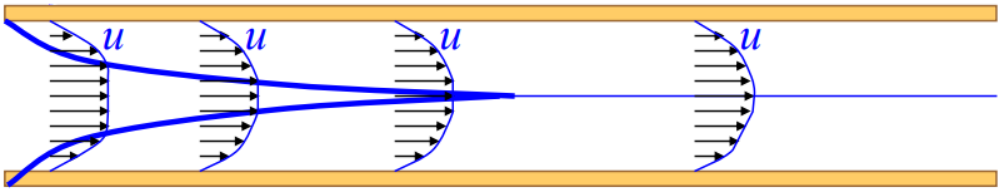

Figure 15: Boundary layer in an internal flow [35]

Then, there will be 7 "pipes" with a rectangular cross section of 1x98 mm and a longitude of 231 mm, which are represented in Figure 16 by green rectangles. The hydraulic diameter of these non-circular "pipes" is computed using Equation 11, where A is the cross section area and P the perimeter.

$$D_H = \frac{4\ A}{P} = \frac{4 \cdot 1 \cdot 98}{2 \cdot 1 + 2 \cdot 98} = 1.9798 \text{ mm} \tag{11}$$

Regarding the mass flow entering the casing, it is set to be the same as the mass flow entering one plate in Section 3.5. In that case, the mass flow was 1.25 kg/s for the whole refrigeration system, which means that each one of the 6 plates had a mass flow of 0.2083 kg/s. This is the mass flow that will enter into the casing, and will split up between the 7 "pipes", having a mass flow of 0.0298 kg/s in each individual pipe.

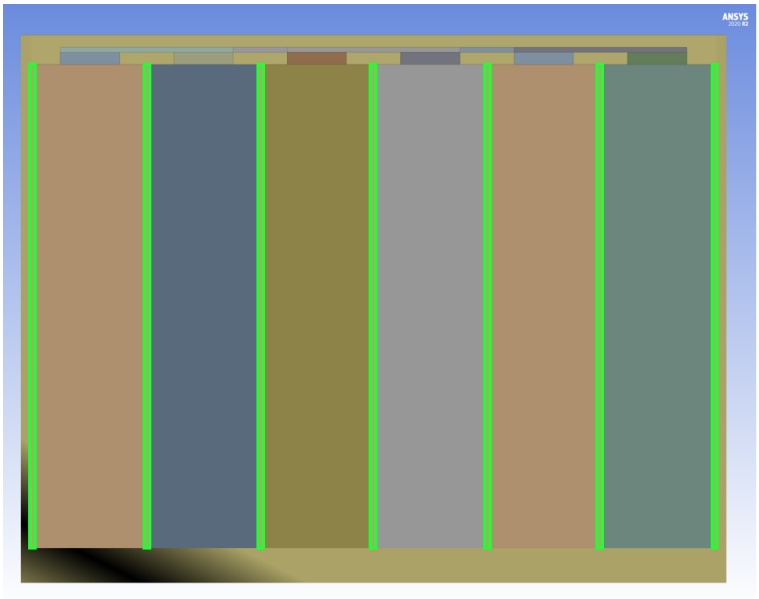

Figure 16: Cross-section view of the rectangular "pipes" between the cells

Now, knowing the mass flow that goes through each "pipe" and considering them as a circular tube using the hydraulic diameter D_H as the characteristic length, the Reynolds number is calculated using Equation 12. In internal flows, the transition between the laminar and turbulent regime is considered to be at $Re \approx 2500$, and a full turbulent flow at $Re \approx 10^4$. For this reason, the flow is considered to be turbulent.

$$Re_D = \frac{\rho\ u_\infty\ D_H}{\mu} = \frac{4\ \dot{m}}{\pi\ D_H\ \mu} = 1.795 \cdot 10^4 \tag{12}$$

Given that, the **Chilton-Colburn analogy** can be used (Equation 13). This analogy is very useful to obtain a good first approximation of the Nusselt number for a fully developed turbulent flow.

$$\frac{Cf}{2} = \frac{f}{8} = \frac{Nu_D}{Re_D \cdot Pr} \cdot Pr^{2/3} \tag{13}$$

Knowing that the friction factor for smooth pipes is $f = 0.184 \cdot Re^{-1/5}$ for $Re < 2 \cdot 10^4$, Equation 13 can be developed into a more convenient expression to calculate the Nusselt number.

$$Nu_D = 0.023 \cdot Re_D^{4/5} \cdot Pr^{1/3} \tag{14}$$

Another way to obtain the Nusselt number is using some experimental correlations based on the previous equation. These are: the Dittus-Bolter correlation, the Sieder & Tate correlation, and the Gnielinski correlation.

The **Dittus-Bolter correlation** (Equation 15) can be used for flows with $0.7 < Pr < 160$, $Re > 10^4$ and $L > 10D$. All these conditions are fulfilled.

$$Nu_D = 0.023 \cdot Re_D^{0.8} \cdot Pr^{0.3} \tag{15}$$

The **Sieder & Tate correlation** (Equation 16) can be used for flows with $0.7 < Pr < 16700$, and $L > 10D$. All these conditions are fulfilled.

$$Nu_D = 0.027 \cdot Re_D^{0.8} \cdot Pr^{1/3} \tag{16}$$

The **Gnielinski correlation** (Equation 17) can be used for flows with $0.5 < Pr < 2000$, and $3000 < Re < 5 \cdot 10^6$. All these conditions are also fulfilled. This correlation is especially made for the range of $2300 < Re < 10^4$, since the previous correlations can introduce some errors in that range.

$$Nu_D = \frac{\frac{f}{8} \cdot (Re_D - 1000) \cdot Pr}{1 + 2.7 \cdot (f/8)^{1/2} \cdot (Pr^{2/3} - 1)} \tag{17}$$

Finally, once the Nusselt number is known, the **convective heat transfer coefficient** can be obtained by solving it from Equation 10.

$$h = \frac{Nu_D \cdot k}{D_H} \tag{18}$$

The results of the Nusselt number and h obtained by using the different correlations are included in Table 9.

	Chilton-Colburn	**Dittus-Bolter**	**Sieder & Tate**	**Gnielinski**
Nu [-]	154.952	140.497	181.9	535.72
h [W/(m^2·K)]	5002.664	4535.974	5872.693	17295.893

Table 9: Results of the Nusselt number and h

From Table 9, some conclusions can be drawn. In the first place, it is noticeable that the Gnielinski correlation differs significantly from the rest, predicting a substantially higher value. This might be due to the fact that this correlation is mostly used in the range of $2300 < Re < 10^4$, and the problem studied is outside this range. Thus, this correlation can be dismissed.

Nevertheless, the other three equations predict similar values of Nu and h. For safety, the highest and lowest values of h are going to be discarded, in an attempt to be neither too optimistic nor pessimistic. As a result, the values obtained with the **Chilton-Colburn analogy** are the ones used. On the other hand, the analogy is made to predict the Nusselt number within a fully developed flow, and does not take into account the entrance zone, where the Nusselt number is higher. But the Nusselt number can be corrected using Equation 19 to consider the entrance zone, and the final value of h is calculated.

$$Nu_D = Nu_{D\text{developed}} \cdot \left(1 + \frac{1}{(L/D)^{2/3}}\right) = 161.441 \tag{19}$$

$$h = \frac{Nu_D \cdot k}{D_H} = 5212.175 \text{ W}/(\text{m}^2 \cdot \text{K}) \tag{20}$$

Then, the value for the heat transfer coefficient $\boldsymbol{h = 5212.175 \text{ W}/(\text{m}^2 \cdot \text{K})}$ is the one chosen to simulate the behavior of the immersion refrigerated battery module.

4 Results

4.1 ANSYS Default Battery Model

4.1.1 Non-refrigerated Battery Module

The global temperature contours for the non-refrigerated ANSYS default battery are presented in Figure 17. The temperature distribution in the module is stratified. The highest temperatures can be found at the upper part close to the tabs, and the lowest ones at the bottom (Figure 17a), resulting in maximum temperature difference within the cells of around 16 K. This behavior is produced because the cells are directly touching the casing at the bottom, which is in contact with the colder ambient temperature and has a lower temperature than the battery. As a result, part of the heat produced is lost by conduction through the bottom of the casing. Thus, the temperature at the bottom of the casing increases until reaching the cells bottom one, as seen in Figure 17a. On the other hand, at the top part, the cells do not touch the casing, causing that the heat generated is not properly evacuated, and therefore producing a high temperature increase.

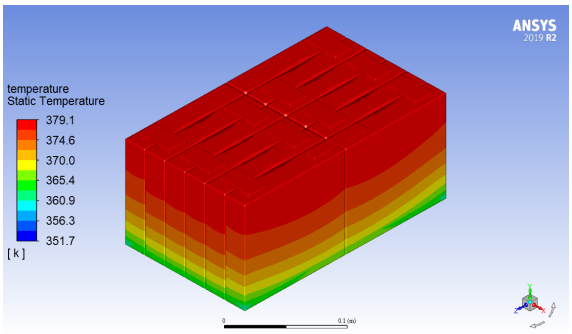

(a) Isometric view of temperature contours of the non-refrigerated module - internal

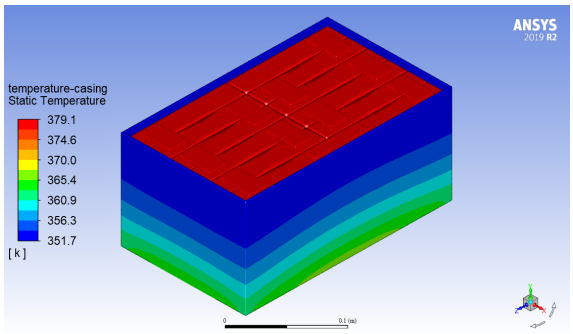

(b) Isometric view of temperature contours of the non-refrigerated module - external

Figure 17: Temperature contours for the non-refrigerated ANSYS battery at 800 s [12]

In Figure 18, the evolution of some variables during the discharge of the batteries is presented. In Figures 18a and 18b, the discharge process can be appreciated. The battery is fully charged, so the SOC starts at 1 and both SOC and voltage start decreasing. The module is subjected to a 4C discharge until the cut-off voltage of the battery is reached, which happens after 813.1 seconds. In Figures 18c and 18d, the total heat generated by the module and the maximum temperature reached within the module are shown, respectively. It can be seen that the temperature increases almost linearly, with a rate of 0.1 K/s, until reaching a final temperature around 380 K (107 °C).

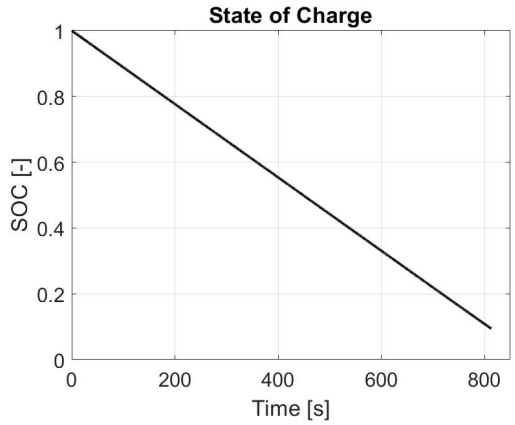

(a) SOC of the module

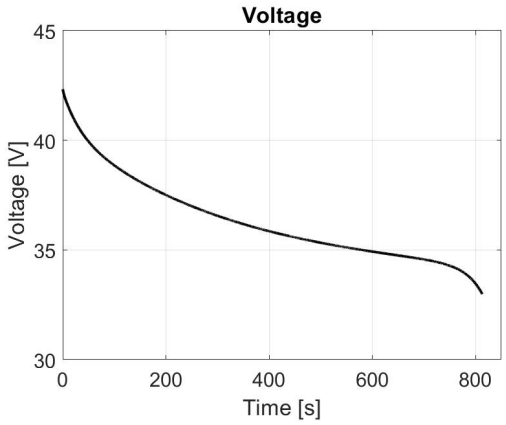

(b) Voltage of the module

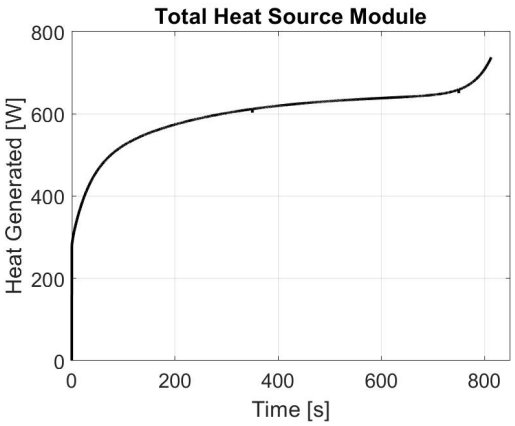

(c) Total heat generation of the module

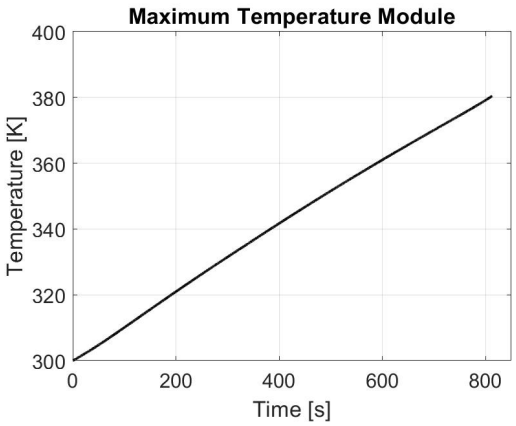

(d) Maximum temperature of the module

Figure 18: Results of a 4C discharge of the non-refrigerated ANSYS battery [12]

4.1.2 Cold-plate Refrigerated Battery Module

In this section, the results from the simulation of the cold-plate refrigerated ANSYS default battery module are exposed. During this calculation, different variables were tracked, and are illustrated in Figure 19. These plots contain the results from the two simulations performed: one with an inlet mass flow of 0.735 m/s and another with an inlet mass flow of 1.47 m/s. Additionally, some of them also contain the previous results from the non-refrigerated case, to facilitate the comparison of the different cases.

In the first place, Figure 19a depicts the total heat production ($\dot{Q}_{\text{generated}}$) of the module, which is clearly almost equal for the three different simulations. Figure 19b shows that, all the heat transmitted by the module to the casing, and then to the cooling plate (refrigeration body), is being extracted through the fluid ($\dot{Q}_{\text{extracted}}$). The concept of Active Cooling (AC) is introduced in Figure 19c. It is defined as the proportion of heat removed by the cooling fluid to heat generated by the module, and it assesses the efficiency with which the refrigeration system extracts heat

$$AC = \frac{\dot{Q}_{\text{extracted}}}{\dot{Q}_{\text{generated}}} \cdot 100 \tag{21}$$

The AC value is primarily determined by the heat flow, since the heat generated behaves slightly sloped throughout the majority of the discharge process. During the first 200 seconds of the discharge, the cold-plate system is able to extract only 40% of the heat generated. This, translated into temperature (Figure 19d), results in a high temperature increase of the module, as if no refrigeration system was used. From that point, the AC continues increasing until reaching a value around 70% near the end of the discharge. As a result, the temperature increase slows down, obtaining a final maximum temperature of the module of 357 K (84 °C), and a decrease around 23 K with respect to the non-refrigerated case. Despite the cooling, however, the maximum temperature attained at the end of the discharge is still too high for the battery to work properly, since it exceeds the maximum operating temperature of 45 °C (see Table 2).

Regarding the differences introduced by changing the inlet mass flow, it can be seen that the heat extracted, active cooling, and maximum temperature of the module are really similar for both cases. In Figure 19e, it can be appreciated that by reducing the inlet mass flow, the fluid temperature increases. This is due to the longer residence time of the fluid, which has more time to be heated. Nevertheless, it does not have enough time to see large differences on the maximum and average temperature of the outlet at the end of the discharge, which are only of 0.635 °C and 0.296 °C, respectively. This explains why the previous mentioned variables do not show significant differences between them.

Lastly, in Figure 19f the SOC and voltage during the discharge of the battery module are included. The refrigerated module behaves as expected, and no perceptible differences were found between the non-refrigerated case and the two simulations of the indirectly refrigerated module. Therefore, only one curve for each variable has been drawn.

As for the temperature distribution for the refrigerated module displayed in Figure 20, the temperature of the casing is no longer stratified and a more uniform contour is obtained, whereas the temperature distribution of the batteries is still layered. As it has just been said, the cooling system manages to lower the maximum temperature of the module to 357.4 K. On the other hand, the temperature gradient within the cells increases, having a maximum temperature difference around 50 K between their upper and lower parts.

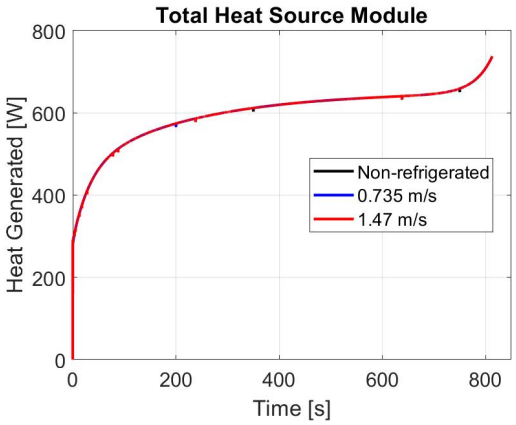

(a) Total heat generation of the module

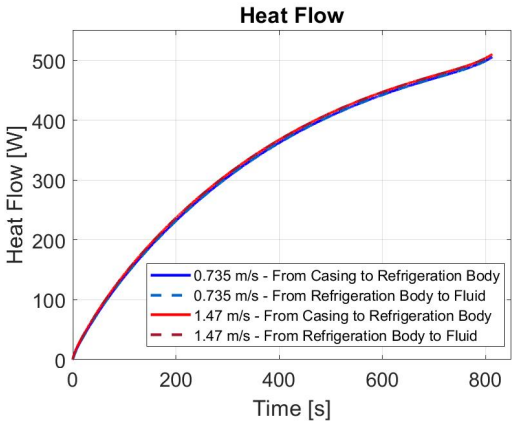

(b) Heat flow from the casing to the fluid

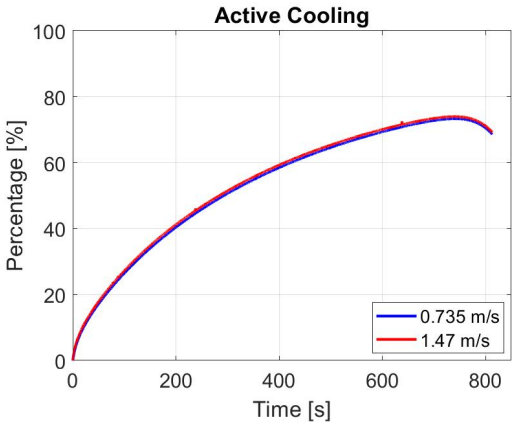

(c) Active cooling

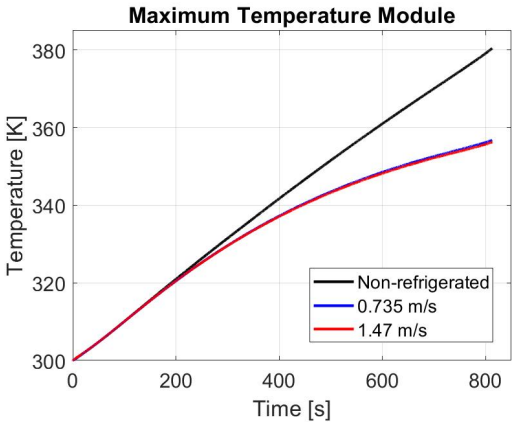

(d) Maximum temperature of the module

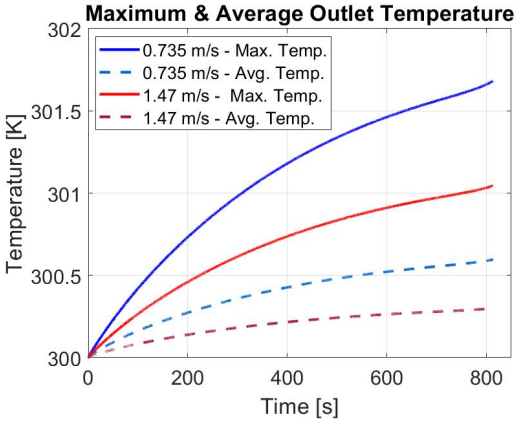

(e) Max. and avg. temperature at the fluid outlet

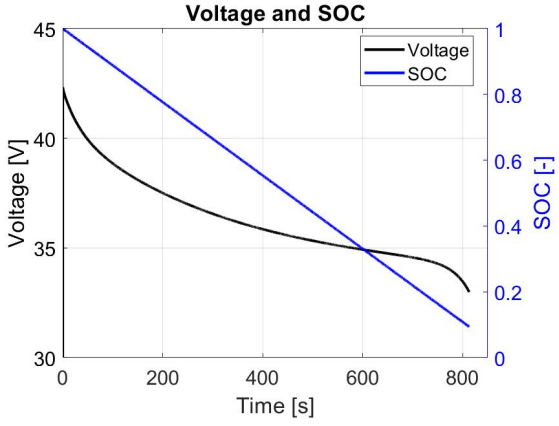

(f) Voltage and SOC of the module

Figure 19: Results of a 4C discharge of the cold-plate refrigerated ANSYS battery

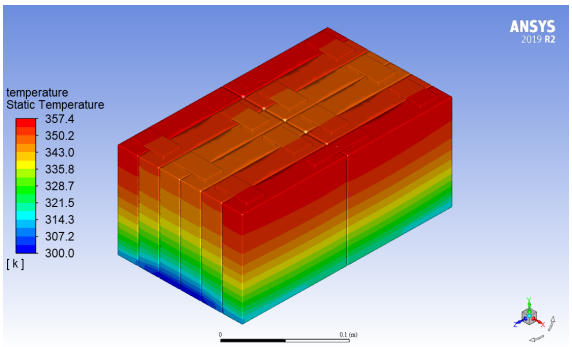

(a) Isometric view of temperature contours of the indirectly refrigerated module - internal

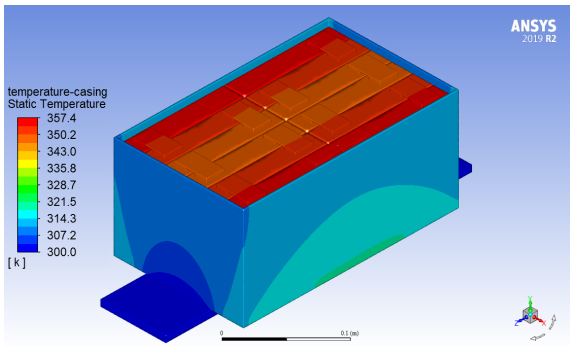

(b) Isometric view of temperature contours of the indirectly refrigerated module - external

Figure 20: Temperature contours for the cold-plate refrigerated ANSYS battery at 800 s - 0.735 m/s

4.1.3 Immersion Refrigerated Battery Module

The results from the simulation of the immersion refrigerated ANSYS default battery module are displayed in Figure 21. These plots contain the results from the simulation performed, and previous results from the non-refrigerated and cold-plate cases.

Figures 21a, 21b and 21c show that the SOC, voltage and heat production remains equal for the three cases. Since the ECM parameters of the ANSYS default battery model only depend on the SOC, it is clear why all these characteristic properties of the battery do not change from one simulation to another.

On the contrary, the temperature of the cells has a completely different behavior, as seen in Figures 21d and 22. In this case, the cooling liquid is able to extract a lot of heat from the batteries. The temperature of the cells increases to 300.65 K at the beginning of the simulation and then it remains constant until the end of the discharge. With respect to the temperature distribution, it can be seen that the stratified behavior has completely disappeared, and a more homogeneous cooling is achieved. It is interesting to remark that now, the highest temperatures are achieved at the bottom part of the cells, given that the batteries are placed inside the 5 mm spacers of the casing and no convection is produced here.

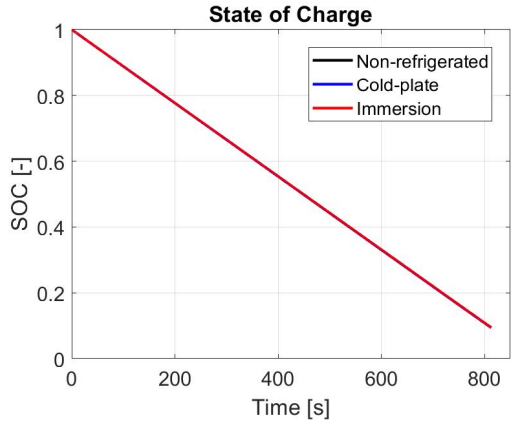

(a) SOC of the module

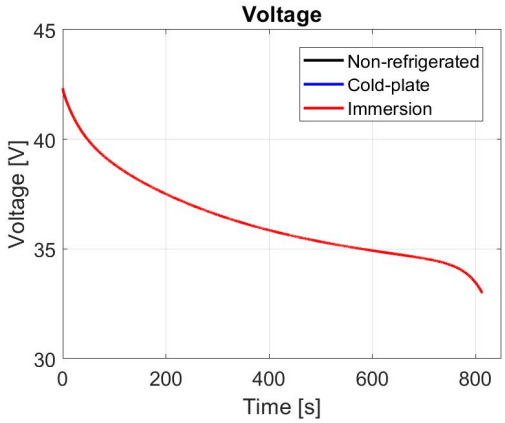

(b) Voltage of the module

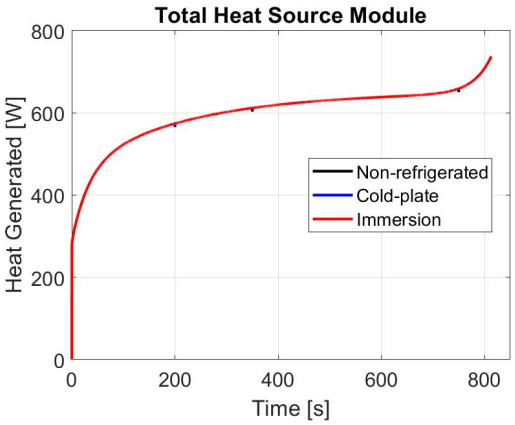

(c) Total heat generation of the module

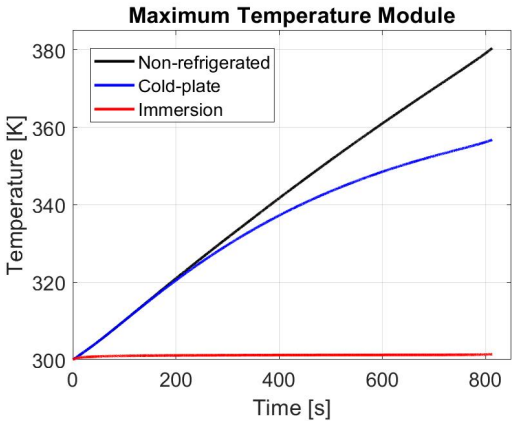

(d) Maximum temperature of the module

Figure 21: Results of a 4C discharge of the immersion refrigerated ANSYS battery

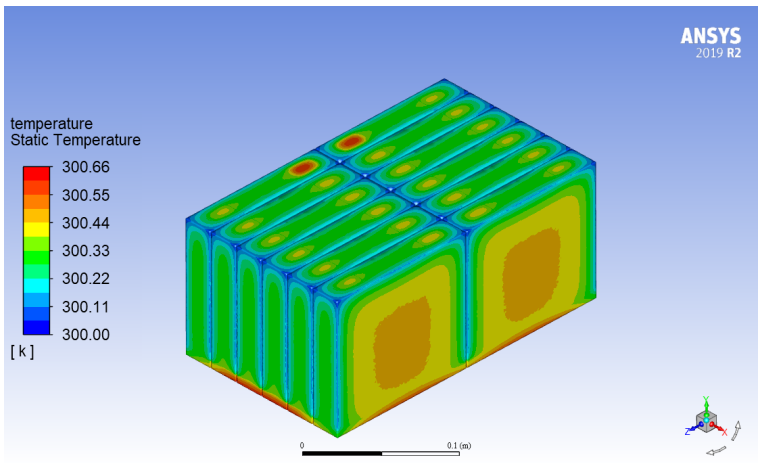

Figure 22: Temperature contour for the immersion refrigerated ANSYS battery at 800 s

4.2 Toshiba SCiB^{TM} Model

In this section, the analysis of the results is repeated, now for the Toshiba SCiB^{TM} model, and they are compared to the results from Section 4.1.

4.2.1 Non-refrigerated Battery Module

The global temperature contours for the non-refrigerated Toshiba SCiB^{TM} are presented in Figure 23. The temperature distribution of the module is similar to the ANSYS default battery case: a stratified behavior, with higher temperatures at the upper part and lower temperatures at the bottom. The maximum temperature difference within the cells is around 2 K, but higher temperatures can be found within the tab zones and busbars.

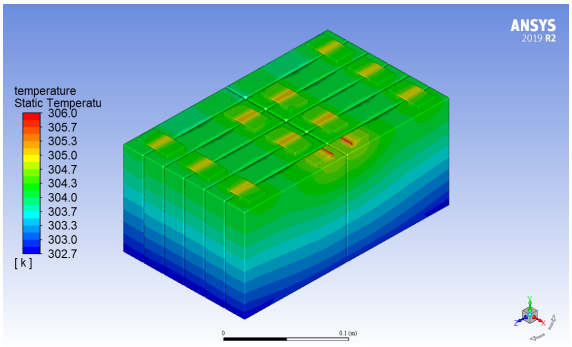

(a) Isometric view of temperature contours of the non-refrigerated module - internal

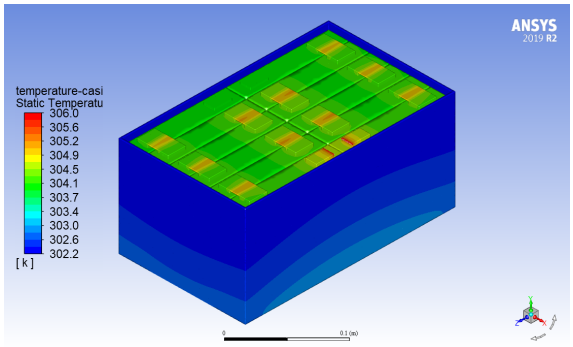

(b) Isometric view of temperature contours of the non-refrigerated module - external

Figure 23: Temperature contours for the non-refrigerated Toshiba SCiB^{TM} at 800 s

In Figure 24, the evolution of the SOC, voltage, heat generated and maximum temperature of the cells is presented. In Figure 24c, it can be seen that the heat generated during most of the discharge process is around 30 W, which is considerably smaller than the 600 W generated by the ANSYS default battery. Therefore, the temperatures achieved by the Toshiba SCiB^{TM} are noticeably lower, with a maximum temperature at the end of the discharge of 305 K (32°C). This value is already inside the operating temperature range of the battery (see Table 4).

4.2.2 Cold-plate Refrigerated Battery Module

The results from the simulation of the cold-plate refrigerated Toshiba SCiB^{TM} module are exposed in Figure 25. As in Section 4.1.2, the plots contain the results from the 0.735 m/s and 1.47 m/s inlet mass flow simulations, and some also contain the results from the non-refrigerated case.

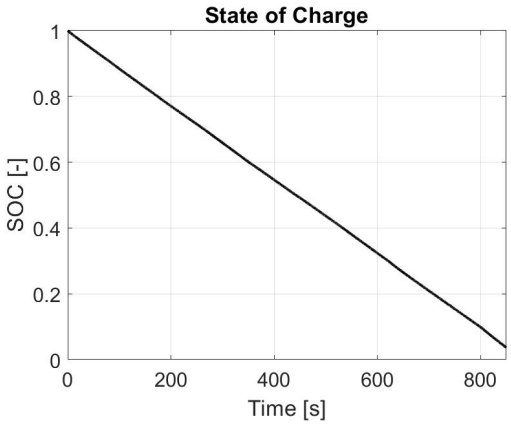

(a) SOC of the module

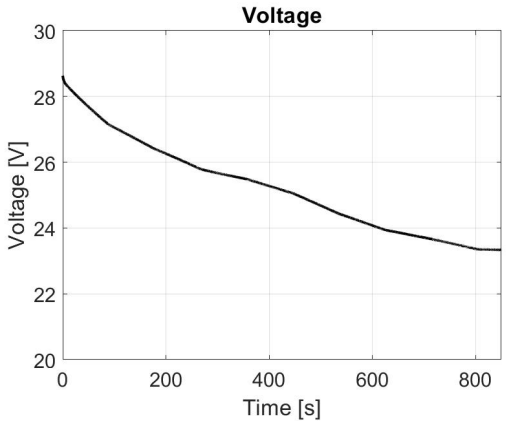

(b) Voltage of the module

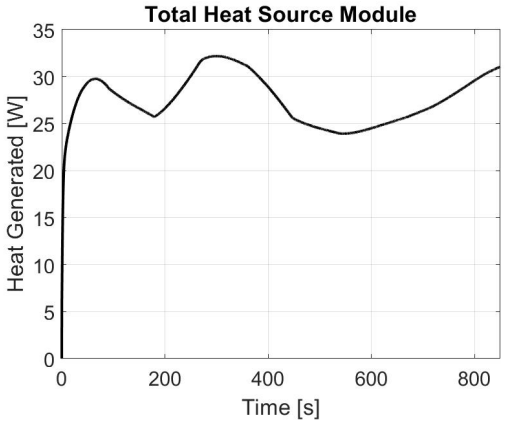

(c) Total heat generation of the module

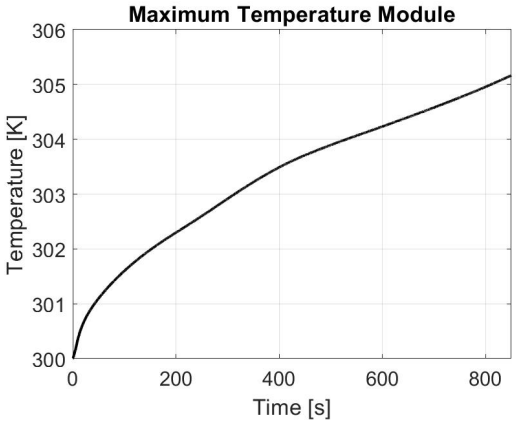

(d) Maximum temperature of the module

Figure 24: Results of a 4C discharge of the non-refrigerated Toshiba SCiB^{TM}

The first thing that must be said is that, once again, the differences introduced by reducing the inlet mass flow are negligible. So, from now on, both simulations will be analysed as a unique case.

The most interesting result is the maximum temperature of the battery cells (Figure 25d). It can be appreciated that the cold-plate helps extracting the heat from the batteries, and the final temperature decreases approximately 1 K. This change in temperature may be the cause of the little differences in the heat generated (Figure 25a), since the ECM parameters used for this battery depend on the SOC, but also on temperature (see Appendix A).

Concerning the temperature distribution displayed in Figure 26, the behavior is similar to the one experienced by the ANSYS default battery: the casing temperature becomes more uniform, whereas the temperature contour of the cells is still layered. The temperature difference between the upper and lower parts increases, but only up to 3 K.

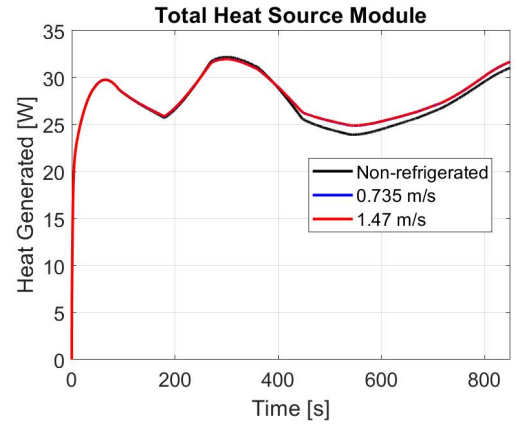

(a) Total heat generation of the module

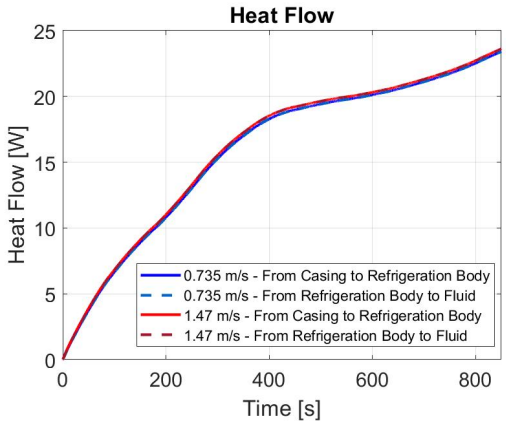

(b) Heat flow from the casing to the fluid

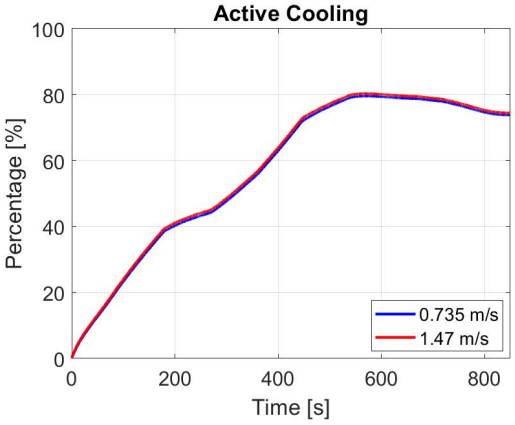

(c) Active cooling

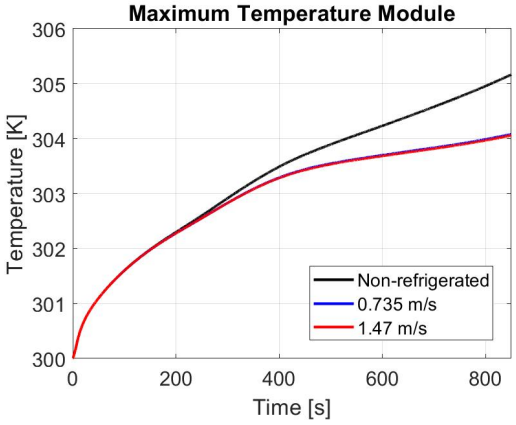

(d) Maximum temperature of the module

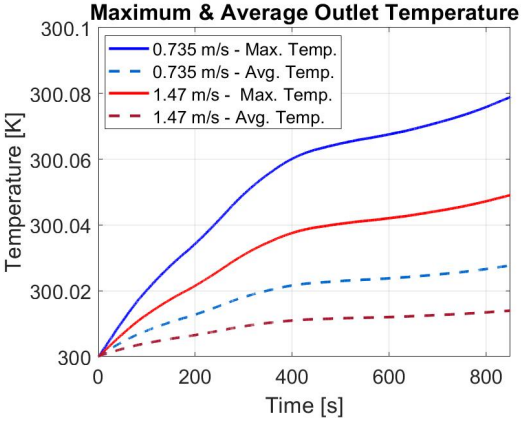

(e) Max. and avg. temperature at the fluid outlet

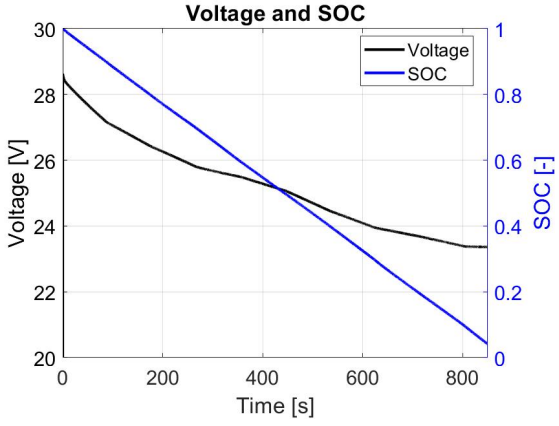

(f) Voltage and SOC of the module

Figure 25: Results of a 4C discharge of the cold-plate refrigerated Toshiba SCiB^{TM}

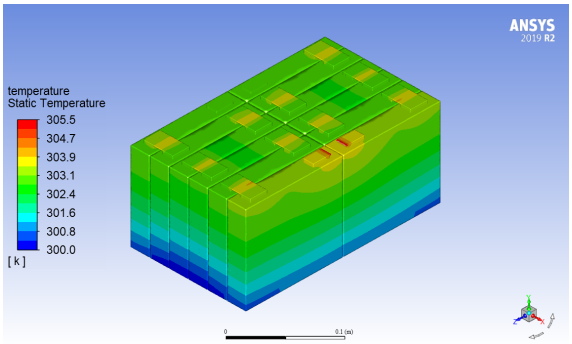

(a) Isometric view of temperature contours of the indirectly refrigerated module - internal

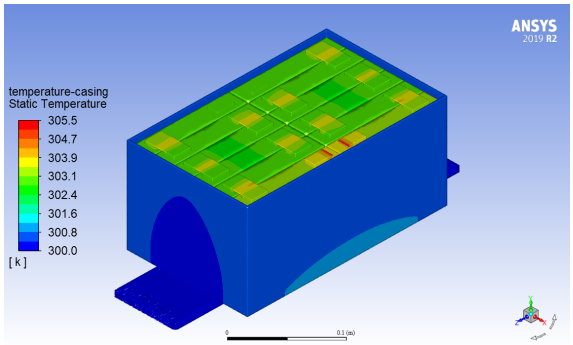

(b) Isometric view of temperature contours of the indirectly refrigerated module - external

Figure 26: Temperature contours for the cold-plate refrigerated Toshiba SCiB^{TM} at 800 s - 0.735 m/s

4.2.3 Immersion Refrigerated Battery Module

The results from the simulation of the immersion refrigerated Toshiba SCiB^{TM} are displayed in Figure 27. It contains the outcome from the immersion case calculation, as well as the ones from the non-refrigerated and cold-plate cases.

In this case, Figures 27a and 27b show that the values of the SOC and voltage are equivalent for the three simulations. The evolution of the heat generated is similar in all cases, but not equal, due to the dependence on temperature of the ECM parameters.

Once again, by using the immersion cooling method, a lot of heat is extracted from the batteries. Consequently, the final temperature of the cells drops 5 K compared to the non-refrigerated case (Figure 27d). This means that the temperature rise is only 0.1 K. With respect to the temperature contour, in Figure 28 it is visible that the temperature is no longer stratified, and a more uniform temperature distribution is obtained.

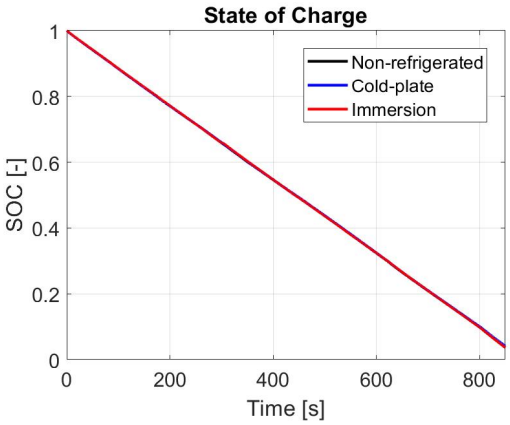

(a) SOC of the module

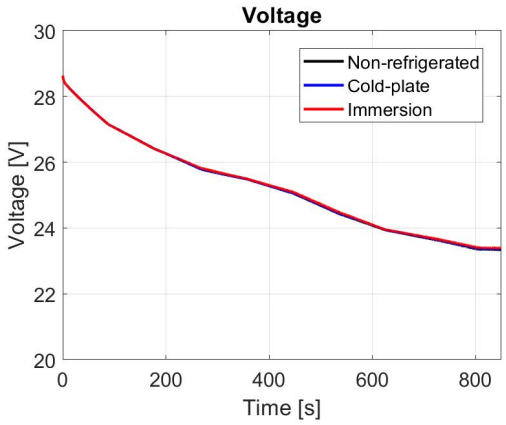

(b) Voltage of the module

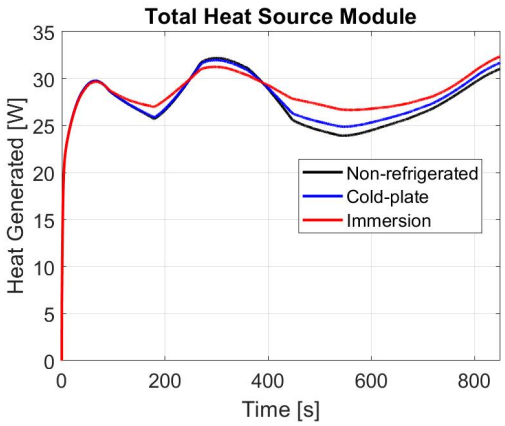

(c) Total heat generation of the module

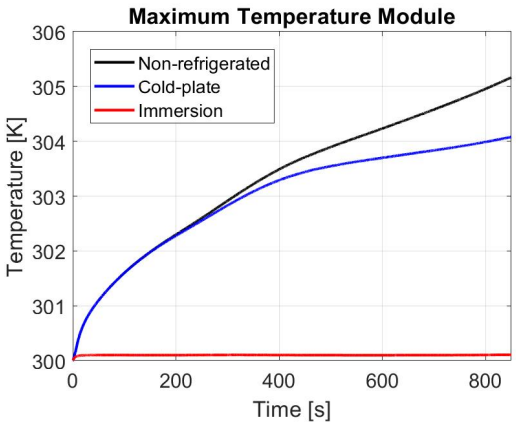

(d) Maximum temperature of the module

Figure 27: Results of a 4C discharge of the immersion refrigerated Toshiba SCiB^{TM}

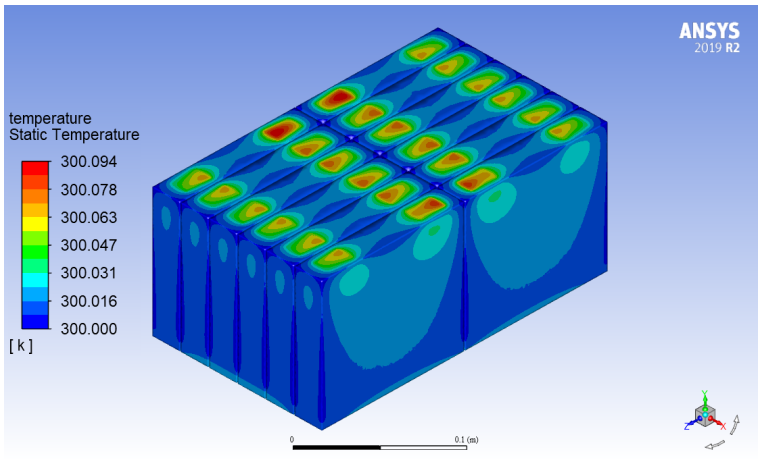

Figure 28: Temperature contour for the immersion refrigerated Toshiba SCiB^{TM} at 800 s

5 Conclusions

In this project, a CFD model for a refrigeration system of a battery module was created. The procedure was separated into three steps: the non-refrigerated module, the cold-plate refrigerated battery module, and the immersion refrigerated battery module.

The first step was to understand the battery add-on module from ANSYS Fluent, which allows to work with different electric models that are quite comparable. After reviewing the literature about the different models, the Equivalent Circuit Model (ECM) was chosen, and the parameters from two different batteries are used: the ANSYS default battery model and the Toshiba SCiB^{TM} model.

The study of the non-refrigerated module allows to observe the electro-thermal behavior of the battery module itself. Despite the addition of a casing, which might be viewed as an additional thermal barrier and a potential way of isolating the batteries, due to the ideal thermal boundary conditions, it actually helps in the dissipation of heat. The heat generated by the cells is extracted through conduction from the lower part of the batteries. The casing, which is made of thin aluminum, absorbs the heat in the form of temperature. The result is a battery module and its casing with a stratified distribution of the temperature, as seen in Figures 17 and 23.

This first study permitted also to look into the differences between the two battery models considered. For instance, the ANSYS default battery generates much more heat than the Toshiba SCiB^{TM}, and the temperature of the cells increase up to 380 K. Therefore, an effective BTMS is needed to decrease its maximum temperature inside its operative temperature range. The temperature of the Toshiba SCiB^{TM}, however, stands inside its recommended temperature range, obtaining a reasonable temperature of 305 K at the end of the discharge. Therefore, if the battery undergoes just a single discharge, a cooling system is not needed. The importance of a BTMS for this battery after a series of continuous charging and discharging cycles is left to be studied in future projects.

The results from the indirect refrigeration system simulation are really interesting. In the study performed by A. Arcila [12], it was concluded that the residence time of the fluid flowing through the cooling plate was to short to efficiently extract the heat generated by the battery module. In this study, the inlet mass flow was reduced in half, thus increasing the residence time of the fluid. Nevertheless, the results from both battery models show that there are no significant differences when decreasing the mass flow. In both cases, the temperature is reduced from its respective non-refrigerated equivalent, which is to be expected, but the temperature drop is unsatisfactory. In the case of the ANSYS default battery, the final temperature is still too high to be inside the operative range. For this reason, it can be concluded that the indirect refrigeration system studied is not efficient enough for the correct operation of the battery, and that its implementation is not worth it.

Given this circumstance, an attempt to find another more efficient BTMS is made, and the immersion refrigeration system is studied. The results from simulating this cooling system

are that the temperature of the module experiences a really small increase of temperature, since the direct contact with the dielectric fluid allows to extract a large amount of heat by convection. As a result, the temperature of the ANSYS default battery never goes beyond its operative limits. Additionally, as the battery cells are surrounded by the cooling liquid, the temperature distribution is more uniform, and the stratified behavior disappears.

However, it is important to remind that the outcome from the last study must been seen just as a gateway to further research, and not as precise results about the real behavior of the immersion refrigeration system. The cooling fluid was simulated considering a convection thermal condition, instead of meshing the whole fluid volume, and the convective heat transfer coefficient h was obtained using experimental correlations. As a future additional study, the influence of the value of h on the solution could be contemplated. All in all, the immersion cooling system seems to be a really promising technology.

6 Project Solicitations

6.1 UPV regulations

In this section, the necessary requirements for the correct execution of the project are described, in accordance with the current regulations applied to the guidelines to a final degree project at the *Universitat Politècnica de València*. The following norms have been directly extracted from the UPV regulations document [36]. As the original language of the document is Spanish, the regulations have been translated to English.

Article 1. Subject matter

The purpose of the current regulations is to establish the general regulatory framework of the conditions governing the registration, assignment, assessment and other aspects of the academic and administrative processing of the Final Degree Projects (*Trabajos Fin de Grado*; hereinafter TFG) and Final Master's Projects (*Trabajos Fin de Máster*; hereinafter TFM) at the *Universitat Politècnica de València* (hereinafter, UPV).

Article 2. Scope of application

1. The present regulations will be applicable to the courses taught by the UPV leading to the achievement of Bachelor's and Master's degrees that are official and valid throughout the Spanish territory (hereinafter, official degrees).

5. The TFG and TFM of the official degrees that enable the exercise of regulated professions will be governed by the provisions of the corresponding Ministerial Order that establishes the requirements for the verification of the degree, without prejudice to the complementary application of what is indicated in the present Framework Legislation.

Article 3. Nature of the TFG and TFM

1. The TFG and TFM must be oriented to the application and evaluation of competences associated to the degree.

2. In the case of the TFG and TFM of degrees that enable the exercise of regulated professions, a professional approach is required. In all other cases, the TFM may have a professional or research approach.

3. The TFG and TFM consists of the completion of an original work or project showing the knowledge, skills and competences acquired by the student throughout their studies and, specifically, the competences associated with the TFG or TFM subject, as indicated in the verification report.

4. The originality of these projects must be understood as an individual part of a comprehensive work developed jointly between students from the same degree or different degrees and the Responsible Structures for the Degrees (*Estructuras Responsables de los Títulos*, hereinafter ERT). In any case, the defense of the TFG and TFM must be individual.

5. The TFG and TFM subject may be defined through formal teaching activities in the form of a seminar, workshop or similar; via autonomous and supervised work of the student; or through a mixture of both.

6. The scope, content and level of demand of the TFG and TFM must be adapted depending on the allocation of ECTS that this subject has received in the verification report [...].

7. Like any other subject in a syllabus, the TFG and TFM must have a Teaching Guide [...].

Article 4. Supervisors

1. When part or all of the ECTS assigned to the subject is organized through autonomous and supervised work, the students will have the guidance of an academic supervisor who will oversee the academic work and will give them support in the administrative management for the completion of their TFG or TFM [...].

4. Supervisors for TFG or TFM may be lecturers who teach in the degree, or have taught in the previous two academic years, or lecturers assigned to the ERT [...].

7. All full-time teaching staff who teach on the degree to which the TFG or TFM corresponds to will be obliged to act as supervisors for the TFG and TFM assigned to them. Part-time teaching staff teaching on the degree may also act as supervisors.

Article 6. Registration for the TFG and TFM

1. In order to be able to register for the TFG or TFM, it will be necessary to be enrolled to all the ECTS pending to complete the studies part of the degree.

2. The registration of the TFG or TFM can be made effective on any date of the course up to 30 calendar days after the date of delivery of the minutes of the first semester [...].

3. The registration of the TFG or TFM in an academic year grants the right to present the work in any of the calls that take place in that academic year, without limit of number of calls, in accordance with the deadlines and procedures established in this Framework Legislation [...].

Article 7. Offer and assignment of TFG and TFM

2. Any student enrolled in the TFG or TFM may submit to the ERT a work proposal endorsed by a supervisor.

3. The Academic Committee of the Degree (*Comisión Académica de Título*, hereinafter CAT) will be responsible for the acceptance of the TFG or TFM proposals taking into account the nature of the work, in accordance with the details presented in article 3 of these regulations, its suitability to the subject of the degree, the estimated duration of the work, and the eligibility of the supervisor as indicated in article 4.

6. The assignment of a TFG or TFM will be valid during the academic year in which the assignment is made and the following academic year [...].

Article 8. Delivery

1. Unless the nature of the work prevents it, prior to the defense and grading of the TFG or TFM, the student must submit to the secretary's office of the ERT the completed project in electronic format, written in Spanish, Valencian or English. The delivery of the work will be done following the procedure established by the Library and Scientific Documentation Area (*Área de Biblioteca y Documentación Científica*), aiming to be included in the institutional repositories of the university.

2. The work submitted will include on the cover page, at least, the author's name; the title; the name of the supervisor and co-supervisor, if applicable; the ERT's name; the degree´s name; the academic year; and the UPV logo. The inclusion of other logos is permitted following the rules for the UPV's logo usage.

5. In order to admit the delivery of a TFG or TFM, the student's transcript must show that he/she has passed all the ECTS credits of their degree, excluding those corresponding to the TFG or TFM itself and, if applicable, those corresponding to external internships or those taken in study exchanges.

6.2 Technical specifications

In this section, the technical specifications necessary for carry out this project are stated.

The use of high-performance computing resources is required to complete the calculations required by the current project. These computer resources may be divided into two categories: hardware and software.

- **Hardware**: Due to the complexity of the calculations to be performed, computing devices with high calculation and memory capacity are required. These are workstations that are connected to the internet, allowing remote access and uninterrupted work without overloading the access terminal. These machines require routine maintenance to ensure that they continue to function flawlessly and efficiently.

- **Software**: The use of computer programs of various types, such as CAD, numerical simulation and post-processing programs, is required to complete the required tasks. The use of commercial software has been chosen, with a view to be able to get technical support in the event of a problem. Therefore, it is needed to have the appropriate licenses in place.

6.2.1 Hardware specifications

A laptop computer and a calculation cluster were used as hardware. The laptop was used as a terminal for accessing the calculation cluster. In addition, it has been used to complete tasks that do not need high levels of performance, such as the setup of the simulations or the data processing. The specifications for the laptop computer and the calculation cluster are described further down.

Laptop computer

The laptop used is an ASUS ZenBook Pro 15 UX580, which has the following specifications:

- Processor: Intel® Core™ i7-8750H @ 2.2 GHz (9M Cache, up to 4.1 GHz)
- RAM memory: 16GB DDR4 2400Mhz on board
- Graphic card: Intel® UHD Graphics 630, NVIDIA® GeForce® GTX 1050, 4GB GDDR5
- Storage unit: 512GB SSD M.2 NVME
- Operating system: Windows 10 Home 64-bit

UPV calculation cluster

The UPV's cluster for massive parallel processing (RIGEL) is made up with [37]:

- 72 Fujitsu BX920S3 type nodes, divided in 4 chassis, each of which is made up of 18 nodes. Each node of the chassis consists of:
  - ⇒ 2 Intel Xeon E5-2450 8c/16T processors of 8 cores and 64 GB/RAM DDR3.
- 56 Bull R424E4 nodes.
  - ⇒ 48 nodes with 2 Intel Xeon E5-2630v3 processors of 8 cores, 2.4 GHz, 20 Mb L3 Cache, and 64 Gb/RAM DDR4.
  - ⇒ 8 nodes with 2 Intel Xeon E5-2630v3 processors of 12 cores, 2.5 GHz, 30 Mb L3 Cache, and 128 Gb/RAM DDR4.
- 27 Dell Power Edge R640 nodes.
  - ⇒ 24 nodes with 2 Intel Xeon Gold 6154 processors of 18 cores, 3 GHz, 25 Mb L3 Cache, and 192 Gb/RAM 2666MT/s DDR.
  - ⇒ 5 nodes with 2 Intel Xeon Gold 6154 processors of 18 cores, 3 GHz, 25 Mb L3 Cache, and 768 Gb/RAM 2666MT/s DDR.

6.2.2 Software specifications

Now, the type of software used is detailed and the use of each program is also specified.

- **Autodesk Fusion 360**

  This Computer Assisted Design (CAD) program was used to create certain sketches of the Toshiba SCiB^{TM} geometry.

- **ANSYS 2019 R2**

  This software was used to import the mesh and build the setup of the different simulations. Some of the applications used from ANSYS 2019 R2 are: ANSYS Workbench, ANSYS Design Modeler, and ANSYS Fluent.

- **MATLAB R2019b**

  This program was essential to create the code that allowed to process the data and present the results.

- **Microsoft Office 365**

  Microsoft Teams tool allowed to have online meetings between the student and the tutor, Microsoft Excel was used during the data processing, and Microsoft Power Point allowed to assemble the slide presentation of the project.

- **Overleaf**

  Overleaf is an online LaTeX editor that was used to write the project memory.

7 Budget

In this section, the total expense of this project is detailed and divided into labour, energy, hardware and software costs.

7.1 Labour costs

Labour costs include expenses related to the hours that both the student and the tutor have dedicated to this work. They are respectively summed up in Tables 10 and 11.

In the case of the student, the wage of a UPV intern was used as a model. It was calculated by taking into account that a scholarship's monthly salary is 400 € for a 3-hour daily work, and typical month with 21 working days.

In the case of the tutor, it has been used as a benchmark the annual remuneration for a UPV-contracted doctor, which is 30139.94 €, and the annual working time is 1750 hours.

Concept	**Hours**	**Cost [€/h]**	**Subtotal [€]**
Meetings	30	6.35	190.48
Documentation and research	30	6.35	190.48
ANSYS tutorial learning	20	6.35	126.98
Simulations setup	40	6.35	253.97
Acquisition of results	35	6.35	222.22
Post-processing	50	6.35	317.46
Memory writing	120	6.35	761.90
Total	325	-	**2063.49**

Table 10: Labour costs corresponding to the student

Concept	**Hours**	**Cost [€/h]**	**Subtotal [€]**
Meetings	30	17.22	516.68
Project revising	10	17.22	172.23
Total	40	-	**688.91**

Table 11: Labour costs corresponding to the tutor

7.2 Energy consumption costs

For the completion of this academic work, one of the most employed tools by the student has been a Personal Computer (PC). As many hours have been spent throughout the entire project, the total expense should include the energetic cost of this laptop. Said PC is an ASUS ZenBook Pro 15 UX580, and its manufacturer [38] states that the power consumption associated to this hardware is 150 W. The total number of hours that the computer has been used equals 325 h, so the total power consumption can be calculated as follows.

$$P_c = 150 \text{ W} \cdot 325 \text{ h} = 48.750 \text{ kWh} \tag{22}$$

Now, it needs to be taken into account that the cost of electric power in Spain depends on the day and even on the hour [39]. The computed average as of September 1st is 0.2193 €/kWh, which allows calculating the total cost of the power consumed by the laptop as:

$$C_P = 48.750 \text{ kWh} \cdot 0.2193 \text{ €/kWh} = \mathbf{10.69} \text{ €} \tag{23}$$

Additionally, the cost of using the UPV calculation cluster RIGEL must also be computed. Each of the 6 simulations calculated in RIGEL has been using 24 processors during an average of 100 hours. Considering that the price of use is 1 cent/hour per processor, a total of **144 €** have been invested.

The total costs associated to the energy consumption are included in Table 12.

Concept	**Subtotal [€]**
PC	10.69
Calculation cluster	144
Total	**154.69**

Table 12: Energy consumption costs

7.3 Hardware costs

Now, the cost associated to the hardware use needs to be estimated. Regarding the student's PC, as it has only been employed for a limited amount of time. The calculated cost will be the one related to the depreciation during that time span. The monthly depreciation cost has been calculated considering that the laptop was bought in 2018 for 1599 €, and a total depreciation period of 8 years. On the other hand, regarding the hardware costs of the calculation cluster RIGEL, the depreciation cost is considered to be included in the 1 cent/hour per processor used before. Therefore, the total costs associated to the hardware are included in Table 13.

Hardware	**Months**	**Cost [€/month]**	**Total [€]**
ASUS ZenBook Pro	8	16.66	**133.25**

Table 13: Hardware costs

7.4 Software costs

Finally, all software licenses employed need to be taken into consideration for computing the total cost of the project. The expenses associated to the software are shown in Table 14.

First of all, the license of the CFD software ANSYS is paid by the amount of time that the simulations have been running. This cost per hour of use of this software is 0.8 €/h.

Regarding MATLAB, it has been used to process the data obtained with the simulations. The cost that the UPV pays for the educational license is of 250 €/year.

In the case of the Microsoft Office 365 programs (Excel, PowerPoint and Teams), the cost that the university pays is 79 € for a 4 year license.

Finally, Fusion 360 was obtained using a free educational license, and Overleaf is a free online tool.

Software	**Usage time**	**License cost**	**Subtotal [€]**
ANSYS 2019 R2	600 h	0.8 €/h	480
MATLAB R2019b	8 months	20.83 €/month	166.67
Microsoft Office 365	8 months	1.65 €/month	13.17
Autodesk Fusion 360	-	0	0
Overleaf	-	0	0
		Total	**659.83**

Table 14: Software costs

7.5 Total costs

The results obtained in previous sections have been summed up in Table 15. To calculate the final budget, an industrial benefit of 5% has been applied, and the Value Added Tax (VAT) of 21% has been added.

Concept	**Cost [€]**
Labour costs	2752.4
Energy consumption costs	154.69
Hardware costs	133.25
Software costs	659.83
Raw total	**3700.17**
Industrial benefit (5%)	185.01
Total with industrial benefit	**3885.18**
VAT (21%)	815.89
Tender budget	**4701.07**

Table 15: Total costs

Therefore, the total raw cost of the project is of:

THREE THOUSAND, SEVEN HUNDRED EUROS WITH SEVENTEEN CENTS

And if industrial benefit is added:

THREE THOUSAND, EIGHT HUNDRED AND EIGHTY-FIVE EUROS WITH EIGHTEEN CENTS

Finally, the tender budget is of:

FOUR THOUSAND, SEVEN HUNDRED AND ONE EUROS WITH SEVEN CENTS

References

[1] U.S. Energy Information Administration. *Monthly Energy Review*. Accessed: 28/08/2021. April 2021.

[2] K.T Chau, Y.S Wong, and C.C Chan. "An overview of energy sources for electric vehicles". In: *Energy Conversion and Management* 40.10 (1999). Accessed: 28/08/2021, pp. 1021–1039. ISSN: 0196-8904. DOI: https://doi.org/10.1016/S0196-8904(99)00021-7. URL: https://www.sciencedirect.com/science/article/pii/S0196890499000217.

[3] R. Spotnitz and J. Franklin. "Abuse behavior of high-power, lithium-ion cells". In: *Journal of Power Sources* 113.1 (2003), pp. 81–100. ISSN: 0378-7753. DOI: https://doi.org/10.1016/S0378-7753(02)00488-3. URL: https://www.sciencedirect.com/science/article/pii/S0378775302004883.

[4] Todd M. Bandhauer, Srinivas Garimella, and Thomas F. Fuller. "A Critical Review of Thermal Issues in Lithium-Ion Batteries". In: *Journal of The Electrochemical Society* 158.3 (2011), R1. DOI: 10.1149/1.3515880. URL: https://doi.org/10.1149/1.3515880.

[5] Qian Wang, Bin Jiang, Bo Li, and Yuying Yan. "A critical review of thermal management models and solutions of lithium-ion batteries for the development of pure electric vehicles". In: *Renewable and Sustainable Energy Reviews* 64 (2016), pp. 106–128. ISSN: 18790690. DOI: 10.1016/j.rser.2016.05.033.

[6] Guodong Xia, Lei Cao, and Guanglong Bi. "A review on battery thermal management in electric vehicle application". In: *Journal of Power Sources* 367 (2017), pp. 90–105. ISSN: 03787753. DOI: 10.1016/j.jpowsour.2017.09.046. URL: https://doi.org/10.1016/j.jpowsour.2017.09.046.

[7] Abu Raihan Mohammad Siddique, Shohel Mahmud, and Bill Van Heyst. "A comprehensive review on a passive (phase change materials) and an active (thermoelectric cooler) battery thermal management system and their limitations". In: *Journal of Power Sources* 401.August (2018), pp. 224–237. ISSN: 03787753. DOI: 10.1016/j.jpowsour.2018.08.094. URL: https://doi.org/10.1016/j.jpowsour.2018.08.094.

[8] Liwu Fan, J. M. Khodadadi, and A. A. Pesaran. "A parametric study on thermal management of an air-cooled lithium-ion battery module for plug-in hybrid electric vehicles". In: *Journal of Power Sources* 238 (2013), pp. 301–312. ISSN: 03787753. DOI: 10.1016/j.jpowsour.2013.03.050. URL: http://dx.doi.org/10.1016/j.jpowsour.2013.03.050.

[9] Ke Li, Jiajia Yan, Haodong Chen, and Qingsong Wang. "Water cooling based strategy for lithium ion battery pack dynamic cycling for thermal management system". In: *Applied Thermal Engineering* 132 (2018), pp. 575–585. ISSN: 13594311. DOI: 10.1016/j.applthermaleng.2017.12.131.

[10] Ian A. Hunt, Yan Zhao, Yatish Patel, and G. J. Offerz. "Surface cooling causes accelerated degradation compared to tab cooling for lithium-ion pouch cells". In: *Journal of the Electrochemical Society* 163.9 (2016), A1846–A4852. ISSN: 19457111. DOI: 10.1149/2.0361609jes.

[11] Yuanwang Deng et al. "Effects of different coolants and cooling strategies on the cooling performance of the power lithium ion battery system: A review". In: *Applied Thermal Engineering* 142.June (2018), pp. 10–29. ISSN: 13594311. DOI: 10.1016/j.applthermaleng.2018.06.043.

[12] Arturo Arcila. *CFD Study of Conjugate Heat Transfer in Battery Cooling Systems for xEV Applications*. 2021.

[13] Chris Woodford. *Batteries*. https://www.explainthatstuff.com/batteries.html. Accessed: 02/08/2021.

[14] Tony R. Kuphaldt. *Lessons in Electric Circuits*. Vol. 1, Direct Current (DC). 2002.

[15] Homestratosphere's Editorial Staff Writers. *19 Different Types of Batteries*. https://www.homestratosphere.com/types-of-batteries/. Accessed: 05/08/2021.

[16] Ali Eftekhari. "Low voltage anode materials for lithium-ion batteries". In: *Energy Storage Materials* 7 (2017), pp. 157–180. ISSN: 2405-8297. DOI: https://doi.org/10.1016/j.ensm.2017.01.009. URL: https://www.sciencedirect.com/science/article/pii/S2405829716303531.

[17] Naoki Nitta, Feixiang Wu, Jung Tae Lee, and Gleb Yushin. "Li-ion battery materials: present and future". In: *Materials Today* 18.5 (2015), pp. 252–264. ISSN: 1369-7021. DOI: https://doi.org/10.1016/j.mattod.2014.10.040. URL: https://www.sciencedirect.com/science/article/pii/S1369702114004118.

[18] ANSTO staff. *Expertise in characterising materials for lithium ion batteries*. https://www.ansto.gov.au/news/expertise-characterising-materials-for-lithium-ion-batteries. Accessed: 02/08/2021.

[19] Isidor Buchmann. *BU-216: Summary Table of Lithium-based Batteries*. https://batteryuniversity.com/article/bu-216-summary-table-of-lithium-based-batteries. Accessed: 06/08/2021. 2019.

[20] Reza Younesi et al. "Lithium salts for advanced lithium batteries: Li–metal, Li–O2, and Li–S". In: *Energy Environ. Sci.* 8 (7 2015), pp. 1905–1922. DOI: 10.1039/C5EE01215E. URL: http://dx.doi.org/10.1039/C5EE01215E.

[21] Toshiba. *Toshiba SCiB Rechargeable Battery Catalog*. https://www.global.toshiba/content/dam/toshiba/ww/products-solutions/battery/scib/pdf/ToshibaRechargeableBatte
en.pdf. Accessed: 06/08/2021. 2020.

[22] Toshiba. *SCiB™ Cells*. https://www.global.toshiba/ww/products-solutions/battery/scib/product/cell.html. Accessed: 07/08/2021. 2019.

[23] Ki Hyun Kwon, Chee Burm Shin, Tae Hyuk Kang, and Chi Su Kim. "A two-dimensional modeling of a lithium-polymer battery". In: *Journal of Power Sources* 163.1 SPEC. ISS. (2006), pp. 151–157. ISSN: 03787753. DOI: 10.1016/j.jpowsour.2006.03.012.

[24] Min Chen and Gabriel A. Rincon-Mora. "Accurate Electrical Battery Model Capable of Predicting Runtime and I-V Performance". In: *IEEE Transactions on Energy Conversion* 21.2 (2006), pp. 504–511.

[25] Marc Doyle, Thomas F. Fuller, and John Newman. "Modeling of Galvanostatic Charge and Discharge of the Lithium/Polymer/Insertion Cell". In: *Journal of The Electrochemical Society* 140.6 (June 1993), pp. 1526–1533. DOI: 10.1149/1.2221597. URL: https://doi.org/10.1149/1.2221597.

[26] Inc. ANSYS. *Ansys Academic Research Fluent, Release 19.2, Help System, Fluent Tutorial, Chapter 25*. Accessed September 9, 2021.

[27] B. Balagopal and M. Chow. "Effect of anode conductivity degradation on the Thevenin Circuit Model of lithium ion batteries". In: *IECON 2016 - 42nd Annual Conference of the IEEE Industrial Electronics Society*. 2016, pp. 2028–2033. DOI: 10.1109/IECON.2016.7793429.

[28] Min Chen and G.A. Rincon-Mora. "Accurate electrical battery model capable of predicting runtime and I-V performance". In: *IEEE Transactions on Energy Conversion* 21.2 (2006), pp. 504–511. DOI: 10.1109/TEC.2006.874229.

[29] Ui Seong Kim et al. "Modeling the Dependence of the Discharge Behavior of a Lithium-Ion Battery on the Environmental Temperature". In: *Journal of The Electrochemical Society* 158.5 (2011), A611. DOI: 10.1149/1.3565179. URL: https://doi.org/10.1149/1.3565179.

[30] Ui Seong Kim, Chee Burm Shin, and Chi-Su Kim. "Effect of electrode configuration on the thermal behavior of a lithium-polymer battery". In: *Journal of Power Sources* 180.2 (2008), pp. 909–916. ISSN: 0378-7753. DOI: https://doi.org/10.1016/j.jpowsour.2007.09.054. URL: https://www.sciencedirect.com/science/article/pii/S0378775307020113.

[31] AUDI AG. *Emotive design and revolutionary technology: the Audi e-tron GT quattro and the Audi RS e-tron GT, Battery and Thermal Management*. 2020. URL: https://www.audi-mediacenter.com/en/emotive-design-and-revolutionary-technologythe-audi-e-tron-gt-quattro-and-the-audi-rs-e-tron-gt-13655/battery-and-thermal-management-13784.

[32] Prahit Dubey, Gautam Pulugundla, and A. K. Srouji. "Direct Comparison of Immersion and Cold-Plate Based Cooling for Automotive Li-Ion Battery Modules". In: *Energies* 14.5 (2021). Accessed: 12/08/2021. ISSN: 1996-1073. DOI: 10.3390/en14051259. URL: https://www.mdpi.com/1996-1073/14/5/1259.

[33] 3M Electronics Markets Materials Division. *3M™ Novec™ 7500 Engineered Fluid*. https://multimedia.3m.com/mws/media/654960/3m-novec-7500-engineered-fluid.pdf. Accessed: 12/08/2021. 2009.

[34] Bunger R. and Day T. Schneider Electric. "Comparison of Dielectric Fluids for Immersive Liquid Cooling of IT Equipment". In: (2020). Accessed: 12/08/2021.

[35] Molina S. and Instituto CMT - Motores Térmicos. *Tema 10: Transferencia de calor por convección (parte II)*. Accessed: 29/03/2020. 2020.

[36] Universitat Politècnica de València. "Normativa Marco de Trabajos Fin de Grado y Fin de Máster". In: (2013).

[37] Mullor Casero R. and Izquierdo Sebastián F. J. *Clúster de Cálculo: Rigel*. `https://wiki.upv.es/confluence/pages/viewpage.action?pageId=264044546`. Accessed: 30/08/2021. 2020.

[38] ASUSTeK Computer Inc. *ZenBook Pro 15 UX580*. `https://www.asus.com/Laptops/For-Home/ZenBook/ZenBook-Pro-15-UX580/techspec/`. Accessed: 31/08/2021.

[39] Selectra. *¿Cuál es el precio del kWh en mercado regulado?* `https://selectra.es/energia/info/que-es/precio-kwh`. Accessed: 31/08/2021.

Appendices

A Toshiba SCiB^{TM} ECM Tables

SOC \ Temp.	298	308	323	333	343
0.05	1.942	1.543	1.1813	1.2341	1.3036
0.1	1.7775	1.367	1.0753	1.0968	1.1339
0.15	1.6874	1.3311	0.9959	1.0546	1.0971
0.2	1.6401	1.2677	0.9493	1.0231	1.0071
0.25	1.5447	1.1832	0.9118	0.9862	1.0076
0.3	1.4761	1.1782	0.8856	0.976	0.992
0.35	1.45	1.1308	0.8808	0.9711	1.019
0.4	1.4186	1.094	0.8706	0.9717	0.9875
0.45	1.4136	1.0998	0.8179	0.9242	0.9136
0.5	1.4033	1.132	0.8608	0.9513	0.9247
0.55	1.4152	1.0953	0.8931	0.9359	0.9996
0.6	1.3246	1.0957	0.8777	0.9308	1
0.65	1.3729	1.0111	0.8567	0.9259	0.9686
0.7	1.3307	0.969	0.8039	0.9263	0.9902
0.75	1.3471	0.9853	0.7886	0.8844	1.0386
0.8	1.3156	1.0656	0.7891	0.922	1.0336
0.85	1.3107	1.0022	0.8001	0.8958	0.9278
0.9	1.3271	1.0133	0.7793	0.907	0.9229
0.95	1.3328	0.9712	0.8169	0.1014	0.9446
1	1.5036	1.078	0.9823	0.8653	1.0567

Table 16: R_S in mΩ as a function of SOC and temperature for the Toshiba SCiB^{TM}

SOC \ Temp.	298	308	323	333	343
0.1	4.0745	3.6650	1.5148	0.9689	1.0881
0.2	3.3093	3.1218	1.0912	0.8691	0.8011
0.3	3.2273	2.3908	0.9231	0.7527	0.1723
0.4	3.3834	1.2334	0.9598	0.7039	0.1755
0.5	3.7958	1.1677	1.1510	0.8262	0.3317
0.6	3.6963	2.5700	1.0172	1.0175	0.0277
0.7	3.9893	3.5114	1.1394	0.7983	0.001
0.8	3.9409	0.05	1.0743	0.8351	0.0001
0.9	3.4658	1.4866	0.8892	0.8727	0.07
1	5.6189	4.2026	5.0387	1.0623	0.875

Table 17: R_1 in mΩ as a function of SOC and temperature for the Toshiba SCiB^{TM}

SOC \ Temp.	298	308	323	333	343
0.1	0.5839	0.3875	0.2893	0.1821	0.1107
0.2	0.4083	0.1821	0.1881	0.1345	0.1286
0.3	0.3964	0.197	0.1107	0.1405	0.1107
0.4	0.3399	0.1673	0.1464	0.078	0.1256
0.5	0.3667	0.1405	0.1494	0.1137	0.1167
0.6	0.3905	2.57	0.1077	0.1494	0.1464
0.7	0.3964	3.5114	0.1941	0.1464	0.1554
0.8	0.4768	0.05	0.1851	0.1464	0.1345
0.9	0.5363	1.4866	0.1941	0.2149	0.1702
1	0.825	4.2026	0.7774	0.1792	0.322

Table 18: R_2 in mΩ as a function of SOC and temperature for the Toshiba SCiB^{TM}

SOC \ Temp.	298	308	323	333	343
0.1	12273.89	11954.89	12210.23	14637.59	12465.1
0.2	15010.13	14243.85	15458.61	17566.25	17439.4
0.3	15510.21	15382.66	16341.11	17810.99	19983.48
0.4	14093.63	11731.13	14669.42	13135.41	20164.8
0.5	13700.84	10186.02	14211.05	12677.53	20665.13
0.6	12027.7	12156.22	11325.32	14967.93	15926.38
0.7	12145.37	13679.38	13744	13422.83	21666.51
0.8	11944.52	10857.06	12327.9	12645.94	26958.86
0.9	12763.85	10399.42	11613.22	14169.1	23945.58
1	8854.56	9685.46	5787.98	12369.13	4190.08

Table 19: C_1 in C as a function of SOC and temperature for the Toshiba SCiB^{TM}

SOC \ Temp.	298	308	323	333	343
0.1	1685.9	2748.4	3399.4	5594	5456
0.2	2400.4	5382.2	5519.3	7542	6822
0.3	2496.9	4999.8	8394	6885	10107
0.4	2835.1	5816.9	6743.3	12502	9416
0.5	2691.8	6874	6736.6	8896	9650
0.6	2497.5	4502.6	8891	3285	10125
0.7	2471.8	3503.2	5319	6691	9605
0.8	2091.4	6308	5279	6857	9050
0.9	1880.2	4108.1	5067	4725	8565
1	1154	1908.4	1497	5679	4376.9

Table 20: C_2 in C as a function of SOC and temperature for the Toshiba SCiB^{TM}

SOC \ Temp.	298	308	323	333	343
0.1	2.1617	2.1449	2.1196	2.106	2.1
0.2	2.1847	2.1719	2.1505	2.1426	2.1349
0.3	2.2059	2.1969	2.1813	2.1696	2.1618
0.4	2.2572	2.2315	2.2179	2.2101	2.2043
0.5	2.3139	2.2896	2.2624	2.2487	2.2468
0.6	2.3478	2.3477	2.3302	2.3127	2.3087
0.7	2.3824	2.363	2.3551	2.3435	2.3396
0.8	2.4288	2.421	2.419	2.4132	2.4054
0.9	2.4966	2.4966	2.4947	2.4869	2.4869
1	2.6033	2.6306	2.6617	2.6247	2.6325

Table 21: V_{OCV} in V as a function of SOC and temperature for the Toshiba SCiB^{TM}